



HAL
open science

Growth of calcium–aluminum-rich inclusions by coagulation and fragmentation in a turbulent protoplanetary disk: Observations and simulations

Sébastien Charnoz, Jérôme Aléon, Noël Chaumard, Kévin Baillié, Esther Taillifet

► **To cite this version:**

Sébastien Charnoz, Jérôme Aléon, Noël Chaumard, Kévin Baillié, Esther Taillifet. Growth of calcium–aluminum-rich inclusions by coagulation and fragmentation in a turbulent protoplanetary disk: Observations and simulations. *Icarus*, 2015, 252, pp.440-453. 10.1016/j.icarus.2015.01.023 . hal-02352269

HAL Id: hal-02352269

<https://hal.science/hal-02352269>

Submitted on 12 Nov 2019

HAL is a multi-disciplinary open access archive for the deposit and dissemination of scientific research documents, whether they are published or not. The documents may come from teaching and research institutions in France or abroad, or from public or private research centers.

L'archive ouverte pluridisciplinaire **HAL**, est destinée au dépôt et à la diffusion de documents scientifiques de niveau recherche, publiés ou non, émanant des établissements d'enseignement et de recherche français ou étrangers, des laboratoires publics ou privés.

1 **Growth of calcium-aluminum-rich inclusions by coagulation**
2 **and fragmentation in a turbulent protoplanetary disk:**
3 **observations and simulations**

4

5 Sébastien CHARNOZ ^{a,b,*}

6 Jérôme ALEON ^c

7 Noël CHAUMARD ^d

8 Kevin BAILLIE ^{a,b}

9 Esther TAILLIFET ^{a,c}

10 (a) Institut de Physique du Globe, Paris, France

11 (b) Laboratoire AIM, Université Paris Diderot /CEA/CNRS, Gif-sur-Yvette Cedex France

12 (c) Centre de Sciences Nucléaires et de Sciences de la Matière, CNRS/IN2P3 – Université Paris Sud,

13 Bâtiment 104, 91405 Orsay campus, France

14 (d) Institut de Minéralogie, de Physique des Matériaux et de Cosmochimie (IMPMC), Sorbonne

15 Universités, Muséum National d’Histoire Naturelle, UPMC Univ. Paris 06, UMR CNRS 7590, IRD UMR

16 206, 61 rue Buffon, F-75005 Paris, France

17 * Corresponding author: charnoz@cea.fr

18

19

20

21 **Abstract**

22 **Whereas it is generally accepted that calcium-aluminum-rich inclusions (CAIs) from chondritic**
23 **meteorites formed in a hot environment in the solar protoplanetary disk, the conditions of their**
24 **formation remain debated. Recent laboratory studies of CAIs have provided new kind of data: their**
25 **size distributions. We report that size distributions of CAIs measured in laboratory from sections of**
26 **carbonaceous chondrites have a power law size distribution with cumulative size exponent between**
27 **-1.7 and -1.9, which translates into cumulative size exponent between -2.5 and -2.8 after correction**
28 **for sectioning. To explain these observations, numerical simulations were run to explore the growth**
29 **of CAIs from micrometer to centimeter sizes, in a hot and turbulent protoplanetary disk through the**
30 **competition of coagulation and fragmentation. We show that the size distributions obtained in**
31 **growth simulations are in agreement with CAIs size distributions in meteorites. We explain the CAI**
32 **sharp cut-off of their size distribution at centimeter sizes as the direct result from the famous**
33 **fragmentation barrier, provided that CAI fragment for impact velocities larger than 10 m/s. The**
34 **growth/destruction timescales of millimeter- and centimeter-sized CAIs is inversely proportional to**
35 **the local dust/gas ratio and is about 10 years at 1300 K and up to 10^4 years at 1670K. This implies**
36 **that the most refractory CAIs are expected to be smaller in size owing to their long growth timescale**
37 **compared to less refractory CAIs. Conversely, the least refractory CAIs could have been recycled**
38 **many times during the CAI production era which may have profound consequences for their**
39 **radiometric age.**

40

41 **1. Introduction**

42 Calcium-aluminum-rich inclusions (CAIs) from chondritic meteorites are the oldest objects formed in
43 the Solar System as indicated by their absolute radiometric ages using the U-Pb chronometer (e.g.
44 Amelin et al. 2010; Bouvier and Wadhwa 2010; Connelly et al. 2012). Understanding their conditions
45 of formation is thus key to unravel the astrophysical conditions in the nascent Solar System. They are
46 widely thought to have formed by gas-solid condensation of a gas of chondritic (i.e. solar) composition,
47 notably for the rock-forming elements (e.g. Grossman 1972, Ebel 2006), but numerous such objects
48 have experienced complex thermal histories, including in some cases multiple partial melting events
49 (e.g. MacPherson 2003; and references therein). Their astrophysical environment of formation has
50 been investigated and it is widely thought they have formed at high pressure ($P > 0.1$ Pa) and high
51 temperature ($T > 1300$ K) in the hot inner region of the solar protoplanetary disk (e.g. Shu et al. 1997,
52 Ciesla 2010). In spite of their common refractory chemistry and isotopic anomalies indicative of
53 formation in a common reservoir, they present a wide diversity of petrographic types and sizes. Their
54 sizes notably span four orders of magnitude from less than $1 \mu\text{m}$ to $\sim 2\text{cm}$, for the smallest corundum
55 (Al_2O_3) grains found in meteorite matrices (e.g. Nakamura et al. 2007, Makide et al. 2009) to the largest
56 so-called type B CAIs (e.g. MacPherson and Grossman 1981, MacPherson et al. 1989), respectively.
57 How CAIs reached such large sizes remains mostly unknown since their growth mechanism has never
58 been investigated in detail. Large rounded cm-sized CAIs have phase relationships indicative of
59 extensive partial melting (e.g. type A and B CAIs, MacPherson and Grossman 1981, Simon et al. 1999,
60 Kita et al. 2012), which obscured their growth mechanism, while other CAIs are aggregates of 10-50
61 μm nodules (such as the fine-grained spinel-rich CAIs; e.g. Krot et al., 2004) and thus may not have
62 been completely melted since they were assembled (see examples on Figure 1). Once partially molten
63 CAIs are also designated as igneous, i.e., crystallized from a silicate melt, or coarse-grained CAIs
64 (designated as CG-CAIs hereafter) and fine-grained aggregates are commonly referred to as fine-
65 grained CAIs (designated as FG-CAIs hereafter). Although nodules from FG-CAIs are thought to have

66 best preserved condensation evidence (e.g. Krot et al. 2004) and may be direct condensates from the
67 gas, laboratory condensation experiments have only produced sub- μm to $\leq 5 \mu\text{m}$ grains to date
68 (Toppani et al. 2006, Takigawa et al. 2012, Tachibana et al. 2014). In addition to the aggregate nature
69 of the FG-CAIs, it was recently realized that several CG-CAIs were in fact compound inclusions made of
70 several lithological units that were initially individual CAIs aggregated to each other before being
71 partially molten to some extent (e.g. El Goresy et al. 2002, Aléon et al. 2007, MacPherson et al. 2012,
72 Ivanova et al. 2012). These observations suggest that coagulation of refractory precursors is a potential
73 mechanism to produce large cm-sized CAIs from initially sub- μm to μm -sized condensates. Conversely,
74 the growth of dust to cm-sized objects in the planet formation regions of protoplanetary disks has
75 been investigated for long (see e.g. Brauer et al., 2008, Birnstiel et al., 2010, Charnoz and Taillifet 2012)
76 and is known to be a rapid mechanism. Dust grains grow from micrometer to millimeter size through
77 surface sticking in a few 10 to 100 years at 1 AU (Brauer et al., 2008, Charnoz and Taillifet 2012). In the
78 present paper, we first report the measurement of size distributions obtained from 4 meteorites from
79 the CAI-rich CV-CK chondrite clan. Then we describe and apply a numerical simulation of grain growth
80 in protoplanetary disks to the case of CAIs growth to determine whether growth by coagulation
81 competing with fragmentation (starting from small precursors) in a hot and turbulent inner disk region
82 (where the pressure and temperature conditions are favorable for CAI formation) is a viable
83 mechanism to produce cm-sized CAIs and the resulting size distribution are compared to laboratory
84 measurements. We also investigate the typical growth time and collisional lifetime of CAIs. The paper
85 is organized as follows: we present laboratory measurements of CAI size distributions and the dust-
86 growth numerical model in section 2 and 3, respectively. In section 4, we present our results from
87 numerical simulations, compare them to laboratory measurements and discuss their implications in
88 the context of planet formation. Our findings are summarized in section 5.

89

90 **2. CAIs size distributions in CV-CK carbonaceous chondrites**

Growth of CAIs

91 Each chondrite group has its own population of CAIs, in terms of size and petrography (e.g. Krot et al.
92 2001). We focused our study to the CV and CV-related CK carbonaceous chondrites, because CAIs in
93 these meteorites are (1) more abundant (up to approximately 15 vol%; e.g. Chaumard et al., 2014), (2)
94 span the full size range from μm - (e.g. Kunihiro et al., 2005) to cm-sizes, and (3) have been extensively
95 studied in the past. To our knowledge, only two studies investigated in details the size distribution of
96 CAIs in CV chondrites (Chaumard et al., 2014; Fisher et al., 2014). Data from Chaumard et al. (2014)
97 were used here to produce new size distributions. The samples investigated here are classified as
98 follows with increasing metamorphic grade: Allende (CV3 Ox.), Northwest Africa (NWA) 779 (CV3),
99 NWA 2900 (classified as a CV3 but similar to CK4 chondrites; see Chaumard et al., 2009, 2014), and
100 Tanezrouft (Tnz) 057 (CK4). Fisher et al. (2014) used 1399 CAIs. Here we used 278 CAIs from Allende,
101 311 CAIs from NWA 779, 223 CAIs from NWA 2900 and 3024 CAIs from Tnz 057, accounting for a total
102 3836 CAIs. Fisher et al. (2014) reported a peak in the size distribution around 150-200 μm for Allende.
103 Chaumard et al. (2014) reported a similar peak for NWA 779 (125–250 μm) and a peak at slightly larger
104 sizes of about 300 μm for NWA 2900 and Tnz 057 but did not observe such a peak for Allende.
105 Chaumard et al. (2014) attribute this peak to the coarsening of the size distributions due to
106 metamorphism on the parent body. Two effects appear to be at the origin of this coarsening: (1) the
107 chemical re-equilibration and (2) recrystallization of CAIs with the surrounding matrix during
108 metamorphism, both effects resulting in a preferential removal of small CAIs relative to the larger ones.
109 Since it has been shown that Allende was significantly metamorphosed (e.g. Bonal et al., 2006), it is
110 possible that the peak at 150-200 μm observed by Fisher et al. (2014) is already a consequence of the
111 parent body metamorphism. As a result, we chose to compare the slopes of the size distributions
112 above 0.2 mm (0.3 mm in Tnz 057, the most metamorphosed meteorite used in this study) to avoid a
113 possible parent body effect due to metamorphism (Table 1).

114 As commonly admitted, Figure 1 shows that cm-sized CAIs are dominated by CG-CAIs. Chaumard et al.
115 (2014) indicate that FG-CAIs from Allende have an equivalent radius mean value of 210 μm and that
116 70% of these FG-CAIs have equivalent radii below 250 μm . These observations indicate that FG-CAIs

Growth of CAIs

117 and CG-CAIs have different size distributions, unmelted FG-CAIs being more abundant for small sizes
118 and partially melted CAIs such as CG-CAIs more abundant for large sizes. Because FG-CAIs are by far
119 the most abundant type of CAIs, their size distribution is likely to be very close to that of the bulk CAI
120 size distribution. By contrast, to establish a size distribution of igneous/CG-CAIs with enough statistics
121 to be representative, a large amount of meteoritic material would be necessary. Although this may be
122 possible using Allende (for which 2 tons of material is available), it is beyond the goal of the present
123 study.

124 The size distribution of CAIs was measured for the 4 CV-CK chondrites listed above (Figure 2). The
125 cumulative exponent of the corresponding size distribution was measured and reported in table 1 in a
126 size range in which the function is approximately linear. As a whole, all meteorites give consistent
127 results suggesting that our results are not significantly affected by parent body metamorphism. The
128 cumulative size distributions of CAIs (number of objects with size larger than r , designated as $N(>r)$)
129 measured in sections display shallow slopes with exponent ranging between -1.7 and -1.99. In addition,
130 the absolute size of the largest CAI differs from one meteorite to another, but the largest sizes are
131 generally up to few mm or cm depending on the meteorite. Note that a bias is possible in the largest
132 sizes due to the amount of surface observed. For instance, although we did not observed cm-sized CAIs
133 in Allende, those are well known to be present and can be easily found on larger slabs of Allende.

134 However, the results mentioned above are size-distributions observed in meteorite sections. As a
135 result, the observed CAI cross-sections do not necessarily correspond to their equatorial sections,
136 resulting in a systematic bias in the estimation of their equivalent radii. Indeed, for each CAI, the real
137 radius (of the three-dimensional object) is never observed, but rather a smaller radius (in general) due
138 to cut effects. In addition, small CAIs have a lower probability than large CAIs to be cut across. The size
139 distribution of CAIs observed in a section is thus biased due to these two competing effects, and one
140 may wonder how the size distribution of CAI in a section relates to the “real” size distribution of CAI in
141 the same meteorite, if we could extract all of them from the meteorite. This question is addressed in

142 Appendix A.1 in the case where the “real” size distribution of CAIs follows a power law (i.e. assuming
143 that $(N>R) \propto r^{-\alpha}$ with α standing for a positive constant). We show that the size distribution of CAIs in
144 a section follows a shallower power law distribution following $N(>R) \propto r^{-\alpha+1}$. So the original size
145 distribution of CAIs is recovered from the observation of the size distribution in a slice by simply
146 subtracting 1 to the measured slope. Inspection of table 1 shows that, for the four meteorites
147 investigated here, the effective slopes of the CAI size distributions range from -2.7 to -2.99 assuming
148 that they behave as a power law, which seems a reasonable approximation far from the size-cutoff
149 after inspection of Figure 2.

150 However, as mentioned in appendix A.2, close to the cut-off radius, in the millimeter range, some
151 deviation from a perfect power law may imply to use a slightly different correction factor. We found
152 using a purely numerical approach (appendix A.2) that in the millimeter size range it is somewhat
153 better to subtract 0.84 to the observed cumulative size distribution to recover the real 3D distribution.
154 So the “real” slopes of the CAI cumulative size distributions would range from -2.54 to -2.83 (Table 1),
155 in the 0.1 mm to 1 mm size range.

156

157 **3. Numerical simulation of CAI growth**

158 After having reported the size distributions of CAIs found in several meteorites, we now investigate if
159 these distributions can be recovered via “classical” models of growth (through surface sticking) in a
160 protoplanetary disk. Since the found distributions (see section 2) are close to distributions at collisional
161 equilibrium (i.e. with differential size distribution with a power-law index close to -3.5) we use the
162 LIDT3D code, that has been validated for the growth of dust in the protoplanetary disk (Charnoz &
163 Taillifet 2012) in a cold environment to the case of CAIs, expected to grow in a high temperature region
164 of the disk. The main originality of the LIDT3D code is that the dust motion in the gas is numerically
165 integrated in 3D in the disk so that we have a good integration of velocities and a good representation

166 of the dust sedimentation process. This is opposed to more classical codes (like Brauer et al., 2008,
167 Birnstiel et al. 2010) in which the dust drift velocity and vertical distribution is analytically computed
168 with some assumptions. This is especially useful when the dust collision timescale gets smaller than
169 the diffusion timescale, so that the dust vertical distribution is prevented from reaching an equilibrium
170 (Charnoz & Taillifet 2012)

171 Whereas the code has been described in details in Charnoz & Taillifet 2012, we recall below its
172 functioning and specificities.

173 **3.1 The gas disk model**

174 We model a small region of the disk, between 0.5 and 0.51 AU. The simulation can thus be considered
175 as local with uniform radial temperature. This region is chosen so that it corresponds approximately to
176 a typical distance from the Sun at which CAIs can form (see e.g. Ciesla, 2010). Thermodynamical
177 conditions were chosen to achieve consistency between astrophysical conditions in the protoplanetary
178 disk and the stability fields of refractory inclusions as derived from equilibrium condensation
179 calculations (e.g. Ebel 2006, Lodders 2003) and from laboratory crystallization experiments (e.g.
180 Stolper 1984, Stolper and Paque 1986). The gas surface density is $\sim 30000 \text{ kg/m}^2$ and the resulting
181 pressure and sound velocity are $\sim 10 \text{ Pa}$ and $\sim 2000 \text{ m/s}$ (and do not change much with temperature).
182 These values correspond to a minimum-mass solar nebula at 0.5 AU heated through viscous and stellar
183 irradiation heating (Baillie and Charnoz, 2014). The gas velocity field (radial and azimuthal velocities)
184 is computed using the formalism of Takeuchi and Lin (2002) assuming an α turbulent parameter of
185 0.01 (Shakura and Sunyaev 1973), which is standard for turbulent protoplanetary disks (Fromang and
186 Nelson, 2009). We assume that the gas radial velocity is independent of the vertical direction Z as many
187 uncertainties remain on the gas flow structure inside a disk (Fromang et al., 2011).

188 We explored a temperature range between 1670 K and 1250 K corresponding to the range of CAI
189 mineral condensation and slightly lower to account for large variations of the local dust/gas ratio. The
190 latter has been determined (1) with the assumption that the bulk dust/gas ratio in the disk is 10^{-2} as

191 commonly admitted and (2) using the fraction of rocky elements condensed at the considered
192 temperature as approximated from equilibrium condensation calculations. We used condensed
193 fractions estimated from Davis and Richter (2005) assuming that the temperatures of condensation
194 were roughly shifted by ~ 100 K in the 10^{-4} bar calculations compared to the 10^{-3} bar case (compilation
195 by Ebel 2006). We assumed that minor changes in the sequence of mineral condensation between the
196 calculations of Yoneda and Grossman 1995, Lodders 2003 and Ebel 2006 are unlikely to change
197 drastically the order of magnitude of the dust/gas ratios used here. In the paper this dust/gas ratio is
198 denoted f .

199 Eight simulations were run to span the range of possible conditions (Table 2). Cases 1 and 2 were run
200 at 1670 K immediately below the expected onset of refractory mineral condensation at 10 Pa (10^{-4} bar)
201 with the condensation of corundum (Al_2O_3) starting at $T_{\text{cond}} \sim 1680$ -1690 K (Lodders, 2003, Ebel 2006).
202 Cases 3 and 4 were run at 1650 K during the condensation of corundum but for a much higher dust/gas
203 ratio (5×10^{-5}). Cases 5 and 6 were run at 1550 K, a somewhat intermediate temperature in the range
204 of CAI mineral condensation temperatures. For each of these three temperatures two simulations
205 were run with $V_{\text{frag}} = 1$ m/s and $V_{\text{frag}} = 10$ m/s to account for the possibility of CAIs being solid or partially
206 molten depending on chemistry (see section 3.3), since the solidus of type B CAIs is in the 1500 K-1660
207 K range (e.g. Stolper 1982, Stolper and Paque 1986, Richter 2004). The last simulations were run at
208 temperatures of 1350 K corresponding to the onset of forsterite condensation (Mg_2SiO_4 , $T_{\text{cond}} \sim 1350$ -
209 1360 K, Lodders 2003, Ebel 2006), the least refractory of primary CAI minerals and of 1250 K, where
210 CAIs can be considered as cold and most olivine, pyroxene and metal as condensed. The corresponding
211 dust/gas ratios are estimated to be 5×10^{-4} and 5×10^{-3} respectively.

212

213 **3.2 Model of particle motion and particle growth**

214 In order to follow the growth of CAIs, we use the code LIDT3D (Charnoz et al., 2011; Charnoz and
215 Taillifet, 2012), which has been designed specifically to track the growth of dust in a turbulent solar

216 nebula. This code allows (i) to integrate the motion of individual particles in the disk and (ii) to compute
 217 the growth and the evolution of the size distribution of objects. A key feature of this code, compared
 218 to other published approaches is that it is a 3D code where vertical diffusion, coagulation,
 219 fragmentation and radial drift are treated concurrently.

220 In the present section, we recall the main aspects of the code. Numerous complementary information
 221 on the code's performances as well as numerous tests may be found in Charnoz and Taillifet 2012. First
 222 the motions of thousands of particles, called tracers, are tracked in a gaseous protoplanetary disk. Each
 223 tracer represents a collection of "real" particles (CAIs in the present case), with a same radius a , and
 224 mass m . Each tracer is evolved in the disk taking into account the gas drag according to the classical
 225 laws:

$$226 \quad \frac{d\vec{v}}{dt} = \frac{\vec{F}_*}{m} - \frac{\vec{v} - \vec{v}_g}{\tau} \quad (1)$$

227 where \vec{F}_* is the gravitational force of the central star, the second term is the gas drag force, \vec{v} is the
 228 particle's velocity, \vec{v}_g the gas velocity and m the particle mass. The dust stopping time τ is in the Epstein
 229 regime:

$$230 \quad \tau = \frac{a\rho_s}{\rho C_s} \quad (2)$$

231 where ρ_s is the CAI density (3500 kg/m³), ρ the gas density and C_s the local sound velocity. When the
 232 particle size becomes comparable to the gas mean free path, we may adopt a different expression for
 233 the gas drag (the Stokes regime). However, whereas the Stokes drag regime is taken into account in
 234 the code, it is never encountered. Accounting for the turbulence is done through a Monte Carlo
 235 procedure, in which a random kick on the position of tracers δr_t is added at each time step to reproduce
 236 the effect of turbulence according to a Gaussian law with mean $\langle \delta r_t \rangle$ and standard deviation σ_r^2 given
 237 by:

$$238 \quad \delta r_T = \begin{cases} \langle \delta r_T \rangle = \frac{D_d}{\rho_g} \frac{\partial \rho_g}{\partial x} dt \\ \sigma_r^2 = 2D_d dt \end{cases} \quad (3)$$

239 where D_d is the effective diffusion coefficient of turbulence and dt the time step. This random walk
 240 closely reproduces the effect of turbulence and many theoretical results have been reproduced with
 241 this procedure (see Charnoz and Taillifet, 2012). D_d depends on the strength of the turbulence as well
 242 as particle size. We use the following prescription for the dust diffusion coefficient (Youdin and
 243 Lithwick, 2007):

$$244 \quad D_d \sim \frac{\alpha c_s^2}{\Omega_k S_c} \quad (4)$$

245 where Ω_k is the local keplerian frequency and α a dimension-less number measuring the strength of
 246 turbulence, in the so-called “ α -disks”. Numerous numerical simulations show that for a magnetized
 247 disk, in hot regions where CAIs may form, α is expected to be ~ 0.001 to 0.01 (see e.g. Fromang and
 248 Nelson, 2009). S_c is the Schmidt number corresponding to the ratio of the dust and gas diffusion
 249 coefficients. Youdin and Lithwick (2007) proposes $S_c = (1 + \Omega_k^2 \tau_s^2)^2 / (1 + 4 \Omega_k^2 \tau_s^2)$ (their equation 37).

250 Once the position and velocity of each tracer is computed individually, the particle growth must be
 251 computed. We adopt a particle-in-a-box approach. Local encounter velocities are computed by doing
 252 local averages in the numerical simulations where we have a direct knowledge of the drift velocities.
 253 Let V_{ij} be the encounter velocities in the disk between CAI of size i and size j . As the turbulence and
 254 thermal motion are not explicitly computed, corrective terms must be added in order to take them
 255 into account:

$$256 \quad V_{ij}^2 = \langle V_i - V_j \rangle^2 + V_{ij, THERM}^2 + V_{ij, TURB}^2 \quad (5)$$

257 The first term is the relative velocity between pairs of particles i and j . This term is directly measured
 258 in the simulation. The second term comes from contribution for thermal random motion between pairs
 259 of particle sizes, it is computed analytically: $V_{ij, THERM}^2 = 8kT(m_i + m_j) / (\pi m_i m_j)$. The third term corresponds
 260 to the contribution from turbulence. It is computed analytically following the formalism of Ormel and
 261 Cuzzi (2007). The magnitudes of the different terms are displayed in Figure 4 where it appears clearly
 262 that the major contribution to relative velocities is the turbulence. Drift velocities contributes to only

263 a few meter per seconds only. Thermal motion has only a negligible contribution, apart from < 0.1
264 micron radius particles. Once the relative velocities are computed, the number of collisions occurring
265 between CAIs of radius a_i and a_j are computed according to the standard particle-in-a-box procedure:

$$266 \quad N_{ij} = V_{ij}\pi(a_i + a_j)^2 dt N_i N_j \quad (6)$$

267 with a_i , a_j standing for the radius of CAI in bins i and j , and N_i and N_j standing for the volume densities
268 of particles with sizes i and j (number of particles per volume unit).

269 **3.3 Fragmentation and coagulation**

270 The law for coagulation and fragmentation is taken from Brauer et al. (2008) and includes coagulation,
271 fragmentation and craterization using a simple procedure. We assume a fixed threshold velocity for
272 fragmentation V_{frag} . If $V_{ij} < V_{\text{frag}}$ then sticking is perfect. If $V_{ij} > V_{\text{frag}}$ then the CAI is destroyed. Fragments
273 are assumed to be distributed according to a power law so that the number of fragments in size range
274 $r \pm dr$ is $dN \propto r^{-3.5} dr$ corresponding (approximately) to a collisional population at equilibrium (if the
275 material strength is size independent, see Dohnanyi 1969, or Birnstiel et al., 2011) or dust grains in the
276 interstellar medium (Mathis et al.1977). A similarly simple procedure is used in several works of dust
277 growth (see e.g., Brauer et al., 2008; Estrada and Cuzzi 2008). This is a very arbitrary procedure but, in
278 the absence of laboratory experiments on the catastrophic disruption of CAIs, it has the advantage to
279 be simple and to depend only on a reduced number of free parameter. We performed several test
280 simulations with constant fragmentation exponents ranging from -2.5 to -4.5 and verified that the
281 observed size distribution exponent when the distribution has reached a steady state, does not
282 sensitively depend on this parameter (variations of magnitude ± 0.1 are observed in the slope exponent
283 only for constant fragmentation exponents ranging from -2.5 to -4.5). This procedure is inspired from
284 dust experiments showing that such a threshold velocity exists and is often in the range of 1 m/s for
285 silicate dust (whereas detailed models show that it depends on the aggregates dust mass ratio, degree
286 of compaction, size of elements etc.; see e.g. Blum and Wurm, 2008). However, since this study is a

287 first investigation of CAIs growth, our choice was to adopt the simplest, though non-trivial, approach
288 in order to easily interpret the results. V_{frag} is unknown for CAIs at high temperature. It may be expected
289 to be larger than V_{frag} for cold solid dust. Indeed, since CAIs grow in a hot environment (> 1500 K) they
290 may become plastic and melt. In consequence they may stick in high impact velocity encounters due
291 to the strong viscosity of the melt (see appendix A of Jacquet 2014): indeed energy can be efficiently
292 evacuated during a collision through plastic deformation. V_{frag} is considered here a free parameter and
293 we tested values of 1 m/s and 10 m/s with the assumption that only above 1500 K a CAI can be
294 plastically deformed owing to partial melting, so that all simulations below 1500 K were run with V_{frag}
295 = 1m/s and simulations above 1500 K were run with both V_{frag} to account for possible variations in the
296 degree of partial melting due to chemistry. The fragmentation velocities used in each run are reported
297 in Table 2.

298 **4. Results of numerical simulations**

299 **4.1 Dynamics of CAIs**

300 Since our simulations are local (they are done in a narrow ring, extending from 0.5 to 0.51 AU, with
301 radial periodic boundary conditions), only the vertical dynamics of CAI may be investigated and not
302 the radial motion. Initially, we assume that CAIs precursor form a population of solid-grains with sizes
303 ranging from 0.01 to 1 μm with a size distribution $(N>R)\propto R^{-2.5}$ and with a total mass computed such as
304 the dust/gas mass ratio corresponds to values reported in Table 2. In a few hundred years CAIs start
305 to grow significantly in all cases considered here. They are efficiently mixed vertically due to
306 turbulence and strong coupling to the gas. We present here the state of the run #5 ($T=1550\text{K}$, $V_{\text{frag}}=10$
307 m/s) that is representative of the other cases. Particles motion is complex and there is a competition
308 between a sedimentation process (due to the loss of energy in the gas drag) and a diffusion process
309 (turbulence) that scatters particles in all directions. This competition results in a close-to-gaussian
310 vertical distribution of particles (see e.g. Fromang and Papaloizou 2006, Charnoz et al., 2011) with the
311 larger particles being more concentrated close to the midplane. The tracers' locations are visible in

312 Figure 3.a. The sedimentation process is very active as we see that the vast majority of dust grains are
313 concentrated close to the midplane, whereas few particles are scattered vertically, due to the strong
314 turbulence. A clearer representation of the spatial distribution of grains is visible in Figure 3.b showing
315 the vertical distribution of grains of different sizes. Millimeter-sized grains (black line) are somewhat
316 more concentrated near the midplane compared to smaller sizes, and the smallest particles
317 (micrometer-sized) are comparatively more scattered vertically Note that the most abundant CAIs are
318 always the smallest.

319 **4.2 Presence of a sharp cut-off radius and implications**

320 We now turn to the size distribution, considering all tracers in the simulations and plotting their size-
321 frequency. We assume that the CAIs population that ends up inside a chondrite has the same size
322 distribution as before its incorporation, when CAIs were still evolving in the gas disk. So we neglect
323 any effect of size-sorting, like aerodynamic drag, that may -or may not- have happened during the
324 formation of chondrites. In Figure 5, we show the time evolution of the size distributions for runs #1
325 to #8. We observe that the size distributions reach a steady state in a time that increases with the
326 temperature (about 10 years for temperature < 1500K, about 100 years for T=1550 K, 1000 years for
327 T=1650 K, and about 10000 years for T=1670 K). This increase is an effect of the decreasing dust/gas
328 ratio with increasing temperature because of partial condensation of refractory species. This time
329 increases approximately inversely with dust/gas ratio, like the collision rate (since the collision
330 timescale is inversely proportional to the dust density). After the size distribution has stabilized to a
331 steady-state shape, the most remarkable feature of the final size distribution is a presence of a sharp
332 cut-off at large size. Such a cut-off is commonly observed in simulations of dust growth (see e.g. Brauer
333 et al., 2008; Birnstiel et al., 2011) and corresponds to the size of objects that encounter the others with
334 an impact speed comparable to the fragmentation velocity V_{frag} . It is the so-called “fragmentation
335 barrier” (see e.g. Brauer et al. 2008 for a detailed description of the fragmentation barrier). This
336 maximum size is somewhat independent of the temperature as the growth of particles through

Growth of CAIs

337 Brownian motion is in general largely negligible (Brauer et al., 2008). Relative velocities are mainly the
338 result of different coupling with the gas flow and turbulence. Figure 4 shows that random velocities
339 are dominated by turbulent motion that is a factor up to 10 larger than the drift velocities of dust with
340 respect to the gas. At about 1 cm radius, relative velocities are about 10 m/s (Figure 4 bottom right)
341 that is our fragmentation velocity in high temperature simulations. This confirms that the sharp-cut-
342 off observed in simulation at large sizes is indeed an effect of the fragmentation barrier. Note however
343 that velocities reported in Figure 4 are measured in the disk midplane. Above the midplane, we have
344 measured that the relative velocities are higher due to the lower stokes number. But this has no
345 significant impact on dust growth as the majority of the dust mass is close to the midplane because of
346 sedimentation.

347 Inspection of Figure 5 shows that the cut-off radius appears to be strongly dependent of V_{frag} : it is about
348 ~ 0.1 mm, ~ 1 cm for $V_{\text{frag}}=1$ m/s and 10 m/s respectively. Since CAIs found in chondritic meteorites are
349 systematically smaller than ~ 2 cm, this observed cut-off suggests that using V_{frag} larger than 1 m/s and
350 up to ~ 10 m/s may be a good guess for producing cm-sized CAIs. However, since random velocities
351 are mainly controlled by turbulence through the value of α , a smaller value of α results in smaller
352 random velocities. So an infinite number of $(V_{\text{frag}}, \alpha)$ combinations may result in the same size-cute-
353 off, since an increase in V_{frag} can be always compensated by an increase of α . For realistic values of α ,
354 we note that magneto-hydrodynamical (MHD) simulations of perfectly magnetized disks indicate that
355 α is always close to 0.01 (Fromang and Nelson 2009), as used here. It is why we retain $V_{\text{frag}}=10$ m/s as
356 an appropriate fragmentation velocity in order to produce a cut-off at about 1cm. Is this value realistic?
357 Laboratory experiments of dust impacts show that solid dust aggregates are generally destroyed for
358 impact velocities in the range of 1 m/s (Blum and Wurm, 2008). However we expect partially molten
359 particles to be much more resistant and survive impacts of several meters per second as they are
360 dominated by their viscosity (see e.g. Jacquet, 2014) in the so-called plastic regime. So our results imply
361 that, if CAIs grew as considered here (competition of coagulation and fragmentation in a turbulent

Growth of CAIs

362 environment close to the Sun), a large CAI size cut-off suggests a plastic regime possibly associated
363 with partial melting during their growth.

364 These basic considerations have implications for the origin and formation mechanisms of the various
365 types of CAIs and for their initial distribution in different chondrite groups. FG-CAIs are found in various
366 abundances in most chondrite groups. Most of them are small, typically up to several 100 μm in their
367 largest dimension, notably in non-CV chondrites. By contrast, extensively molten CAIs such as type B
368 CAIs are systematically large, i.e. in the mm-cm size range and are only found in CV-CK chondrites. The
369 melilite-rich type A CAIs are thought to have been once (at least) partially molten and span a large size
370 range from 100-200 μm to few cm (e.g. Simon et al. 1999, MacPherson 2003). Among these, the so-
371 called fluffy type A CAIs have long been thought to be condensates, or aggregates of condensates
372 (MacPherson and Grossman 1984), but were recently interpreted as being aggregates of smaller
373 partially molten type A CAIs (Rubin 2012). These observations suggest that V_{frag} of ~ 1 m/s might be
374 better to characterize the collisional evolution of FG-CAIs, while larger V_{frag} up to ~ 10 m/s might be
375 relevant for characterizing the collisional evolution of partially to extensively molten inclusions. The
376 largest abundance of FG-CAIs relative to coarse-grained igneous CAIs from CV chondrites (in a number
377 ratio of 20-100 to 1; Chaumard et al., 2014) combined with a V_{frag} of ~ 1 m/s could explain the peak at
378 150-200 μm observed in the size distributions of CAIs in CV chondrites. The larger sizes of igneous CAIs
379 are better accounted for using a V_{frag} in the 10 m/s range, which produces a cut-off in the right size
380 range, i.e. for cm-sized objects. The coincidence between their igneous nature and the need for a larger
381 V_{frag} to explain their size range is consistent with plasticity during a partially molten state as a possible
382 cause of a larger V_{frag} . We note that several igneous CAIs larger than 1 cm with bowl shapes rather than
383 spherical shapes have been “frozen” in a plastically deformed state at high velocities relative to the
384 gas (Ivanova et al., 2014).

385 Still, this does not explain the occurrence of large unmelted FG-CAIs in the several mm size range in CV
386 chondrites for which an alternative explanation may be required. If V_{frag} of 1 m/s best corresponds to

387 FG-CAIs, then a growth in a dynamically quiet environment like a dead-zone could be relevant for these
388 objects. In such a low turbulence environment, it has already been shown that dust grains can
389 efficiently grow up to cm-sizes by coagulation (Charnoz and Taillifet 2012). This may also be a preferred
390 environment for the growth of the large igneous CAIs, although subsequent escape from the dead-
391 zone would be necessary for partial melting and in order to achieve the high velocities relative to the
392 gas required for the bowl shaped CAIs (Ivanova et al., 2014).

393 As far as other chondrite groups are concerned, it is worth noting that most CAIs are usually fine-
394 grained and small, typically below 500 μm in size, which indicates a collisional evolution in agreement
395 with a low V_{frag} closer to the classical $V_{\text{frag}} \sim 1$ m/s. It is well known that different chondrite groups have
396 different populations of CAIs (Krot et al. 2001) indicating accretion of CAIs with different spatial and/or
397 temporal distribution in the protoplanetary disk. Our present dynamical approach does not allow
398 distinguishing between different populations of CAIs with similar size distribution because we use a
399 simple approach (no radial transport, assumption of a minimum mass solar nebula) still we evidence
400 that CAIs sampled by CV-CK chondrites have a different dynamical history compared to other chondrite
401 groups. CV-CK chondrites, and only CV-CK chondrites, preferentially sampled a reservoir of large
402 partially (to extensively) melted CAIs with V_{frag} possibly as large as 10 m/s, as well as large unmelted
403 CAIs which may trace the presence of a dead-zone in the solar protoplanetary disk at the epoch of the
404 accretion of the CV-CK parent body. Note that the existence of a dead-zone and large V_{frag} due to partial
405 melting are not mutually exclusive.

406 **4.3 Shape of the cumulative size distribution**

407 The cumulative size distributions obtained in our simulations for $V_{\text{frag}}=10$ m/s and for different
408 temperatures are presented in Figure 6 and shows a clear linear trend (in log-log plot) reminiscent of
409 the CAI size distribution observed in meteorites (see Figure 2). However, size distributions obtained in
410 simulations of CAI growth do not present the flattening at the small-size end. As discussed in section
411 2, this tendency for a shallower slope at small sizes may be an effect of secondary parent body

412 processes, such as aqueous alteration and/or thermal metamorphism as shown by Chaumard et al.
413 (2014). In order to avoid possible parent body effects on the size distribution, we subsequently
414 compare our simulations with size distributions calculated for CV-CK CAIs larger than 200-300 μm .

415 In our simulations, the exponent of the cumulative size distribution is measured in the radius range
416 from 10^{-5} m to 10^{-3} m, a range in which the slope always appears approximately constant. For all
417 simulations presented in Figure 6, the slope is systematically close to -2.43 with 1 sigma error of about
418 ~ 0.03 . We remind to the reader that a system in fragmentation equilibrium has a cumulative size
419 distribution, $N(>r)$, with an exponential slope close to -2.5 if the material strength does not depend on
420 size (see e.g. Dohnanyi 1969; Hartman et al., 1969; Birnstiel et al., 2011), that is equivalent to a
421 differential mass distribution with $N(<R) \propto r^{-2.5}$.

422 These exponents obtained in our simulations (Table 3) are consistent with values reported in CV-CK
423 chondrites of CAIs size distribution (Table 1), after correction for slicing (see section 2 and Appendix
424 A). However, we note that the range of cumulative slopes observed in chondrites extend from -2.54 to
425 about -2.83, which is slightly steeper than observed in our simulations (about -2.43). This small, but
426 substantial, difference may either result from the over-simplicity of our collisional model, or more
427 simply, from small differences on the precise location of the cut-off radius (about 1 cm) in the size
428 distributions. Indeed we observe that close to the radius-cut off, the slope becomes very steep (< -5)
429 and thus may bias the measured slope toward steeper values. Birnstiel et al. (2011) provides an
430 analytical model of the equilibrium size distribution in case a fragmentation barrier is present.
431 Depending on the growth regime (growth cascade, fragmentation dominated and intermediate)
432 different exponents are found. Considering the intermediate case, applying Eq. 24 of Birnstiel et al.
433 (2011) with the current model parameters (-2.5 for the exponent of fragments size distribution and a
434 collision kernel exponent about -1), the resulting size distribution exponent found is in the range -2.5
435 to -2.7, which is qualitatively consistent with the above results.

436 We have also tested the sensibility of our approach to the assumed exponent of the size distribution
437 using simulations with differential size exponents varying between -4.5 and -2.5. It was found that the
438 final distribution at steady state has always about the same slope, between 0.1 and 1 mm with only
439 very little variation (about -2.45 ± 0.05), whereas the distribution at smaller sizes may be substantially
440 different. This insensitivity of the final size distribution to the assumed slope of the fragments' size
441 distribution is also found in Figure 6.a of Birnstiel et al. (2011) where varying the ξ parameter
442 (exponent of fragments' size distribution) has little influence on the final size distribution at equilibrium
443 below the radius at the fragmentation barrier. This is probably an effect not considered in the analytical
444 model of Birnstiel et al. (2011) such as cratering and erosion, which are found here to be effective
445 processes just below the maximum radius. It seems that the equilibrium slope size distribution is
446 relatively independent of the details of the fragmentation process in a collisional cascade just below
447 the maximum radius (see e.g. Tanaka et al., 1996, Kobayashi & Tanaka 2010).

448 In conclusion, the observation that the size-exponent of CAIs size distribution is close to the collisional
449 equilibrium, may tell us that CAIs have reached collisional steady-state, through many series of
450 coagulation and fragmentation cycles, before being incorporated into chondrites.

451 **4.4 Lifetime of individual CAIs**

452 In addition to the study of global size distributions, our simulations can also be used to shed light on
453 the growth history of individual CAIs.

454 We have computed, for each size bin, the production rate of new bodies by coagulation and
455 fragmentation processes. Our results are reported in Figure 7. Here we insist on the different roles
456 played by coagulation and fragmentation, that both can produce, or remove, new objects in a given
457 size range. Thus, for each size range, a production, or destruction, rate can be associated with either
458 fragmentation or coagulation.

Growth of CAIs

459 To present our results in a physically understandable way, we have plotted in Figure 7 the
460 characteristic production, or destruction, timescale (i.e. the number of objects in a size bin divided by
461 the production or destruction rate). Diamonds indicates a destruction/removal timescale while a cross
462 indicates a production timescale. The black line stands for fragmentation while red line for coagulation.
463 To summarize: for fragmentation (black line), a cross indicates production of fragments in a given size
464 range (due to fragmentation of larger bodies) and a diamond indicates that bodies disappear from a
465 size bin because they are fragmented. For the coagulation regime (red), a cross indicates that a size
466 bin is populated through coagulation of smaller sized objects, whereas a red diamond indicates that
467 the size bin loses material because the material is used for the growth of larger bodies.

468 For all cases, the fragmentation production rate (in black) and coagulation removal rate (in red) are
469 close to each other (with some noisy sharp variations due to lack of resolution of the simulation). This
470 means that the fragmentation process is almost balanced by the coagulation process leading to a
471 steady state size distribution, as observed. The characteristic production timescales range from a few
472 10 to a few 10^4 years depending primarily on temperature (because temperature regulates the
473 dust/gas mass ratio) and to a lesser extent on the size. The lifetime of CAIs at 1650 K is a few 10^3 years
474 for mm to cm sized objects and closer a few 10^2 years for CAIs < 0.1 mm (at the same temperature),
475 when the dust to gas ratio is 5×10^{-5} . It drops to approximately 10-100 years at $T=1350\text{K}$ for a dust to
476 gas ratio of 5×10^{-4} . Only at onset of CAI mineral condensation at very high temperature (1670K), when
477 the dust/gas ratio is very low (5×10^{-6}), the timescales jumps to $\sim 10^4$ years to grow mm to cm-sized CAIs.
478 Ultra-refractory CAIs, such as hibonite-rich CAIs, corundum bearing CAIs or CAIs with ultra-refractory
479 Rare Earth Element abundances, are thus expected to be dominated by a population of smaller objects
480 compared to less refractory CAIs that grew in a denser environment resulting in a shorter growth
481 timescale. This agrees well with observations in chondrites with only one UR-CAI reported to date
482 larger than 1 mm (El Goresy et al. 2002). By contrast, less refractory CAIs are common among mm- to
483 cm-sized CAIs (e.g. type B CAIs or fine-grained spinel-rich inclusions).

Growth of CAIs

484 The period of CAI formation is a matter of debate but could last about 10^3 to 10^5 years (Larsen et al.,
485 2011; Thrane et al., 2006) that is somewhat larger than the growth timescales observed in our
486 numerical simulations. This implies that lower temperature CAIs may have been recycled several times
487 whereas high temperature CAIs may have had just enough time to grow before being extracted from
488 the condensation region. Recent simulations (Taillifet et al., 2014) show that a single CAI takes about
489 ~ 1500 years to escape the production region of CAIs (this region may produce CAIs for 10^5 years, but
490 one individual object could leave it in a shorter time due to turbulent diffusion and gas drag), implying
491 that the material it contains should have been fully processed (i.e. coagulated then fragmented) up to
492 100 times for the least refractory CAIs. These multiple recycling events may have major consequences
493 on our understanding of CAI ages since newly formed condensates will be rapidly assembled with
494 fragments resulting from CAI collisions. The important implications of this effect are that the age of
495 CAI precursors are likely to be biased toward older ages and the restricted period of CAI formation
496 estimated from bulk rock ^{26}Al dating is possibly underestimated. This period has been estimated by
497 various studies to vary between possibly as little as 4 000 years (Larsen et al. 2011) and at most 50 000
498 years (Thrane et al. 2006) depending on the analytical uncertainties of the measurements. Averaging
499 data from several sources, a duration of 24 400 years is taken by Mishra and Chaussidon (2014). The
500 extent of this underestimation strongly depends on the relative efficiencies to produce small dust
501 particles by condensation of new CAI precursors and fragmentation of previous CAI generations. This
502 possible bias on bulk rock ages is a possible explanation for the observed difference between the short
503 period for CAIs precursor formation and the longer period of CAI processing determined from mineral
504 isochrons on individual CAIs (see e.g. Kita et al., 2013; Mishra and Chaussidon 2014). The quantification
505 of this effect is complex and will be addressed in a future paper.

506 This recycling may also scramble and mix the different generations of CAIs populations. One would
507 expect from our model to have fine-grained CAI-like fragments being dominant precursors of both FG-
508 CAIs and coarse-grained igneous inclusions because they are the dominant population of CAIs. But,
509 although it may not be the majority, fragments of igneous CAIs are likely to be present among the

510 precursors of later igneous CAIs due to the recycling process. Such precursors would thus have highly
511 variable thermal histories. Aggregation and coagulation of such diverse precursors is an efficient way
512 to produce very complex CAIs with both chemical and isotopic systematics difficult to understand in
513 simple condensation + evaporation + fractional crystallization models. Growing observations indicate
514 the aggregation of such heterogeneous precursors. The coagulation of at least three types of
515 precursors with different thermal histories including ultra-refractory (UR) inclusions, FUN-CAI like
516 (Fractionated with Unknown Nuclear isotopic anomalies) material and spinel-rich proto-CAIs has been
517 recognized in the compact type A inclusion Efremovka 101.1 (Aléon et al. in prep). The 3N inclusion of
518 the NWA 3118 CV chondrite shows aggregation of multiple CAI precursors, including at least one
519 compact type A, a forsterite-bearing type B, and a small UR inclusion, all three being partially melted
520 (Ivanova et al. 2012). The presence of Ca-bearing forsterite (fo) in fo-rich type B CAIs may be explained
521 by melting and subsequent crystallization of CAI material having accreted a forsterite rich rim (Krot et
522 al., 2014; Bullock et al., 2012) strengthening further the idea that fully formed CAIs are multi-
523 component assemblages. In addition, the study of Ca and Ti isotopic composition of FUN inclusions
524 indicates an isotopic continuum between FUN-CAIs and normal CAIs, which can be easily interpreted
525 as recycling of a variable amount of presolar evaporation residues with large Ca and Ti isotopic
526 anomalies among regular CAI precursors (e.g. Park et al. 2014). Finally, this may also explain the
527 decoupling between various isotopic systems, or between isotopic systems and chemistry, in complex
528 inclusions, such as the evaporated host inclusion of E101.1 which shows decoupling of Mg and Si
529 isotopes (Aléon et al. in prep).

530 **5. Summary and conclusion**

531 We have reported here a first attempt to quantify the collisional growth of CAIs in the disk's inner hot
532 regions by confronting meteoritic observations to numerical simulations. First, we quantified CAI
533 populations observed in sections of primitive chondrites. We found that, after correction for
534 geometrical effects (Appendix A), the observed CAI populations have a power-law size distribution with

Growth of CAIs

535 cumulative size exponent ranging from -2.5 to -2.8 (for CAIs radii ranging from a few 0.1 mm to a few
536 mm) close to the equilibrium value (-2.5) for a collisionally evolved population (see e.g. Dohnanyi 1969
537 for the simple collisional case with no recycling or Birnstiel et al., 2011 for a more refined model with
538 recycling through coagulation and fragmentation of largest sized bodies). In order to understand and
539 interpret these results in the context of planet formation, a dust-growth code was used (LIDT3D
540 described in Charnoz & Taillifet 2012). The growth of CAIs was simulated in a minimum mass solar
541 nebula at 0.5 AU from the proto-Sun at temperatures varying between 1250 and 1670 K. The disk is
542 assumed to be turbulent with $\alpha=0.01$.

543 Our main findings are:

- 544 • Numerical simulations naturally produce power-law distributions of CAIs with cumulative size
545 exponents close to observations and with a sharp size cut-off that results from the so-called
546 “fragmentation barrier”. The fragmentation barrier controls the size of the largest objects.
- 547 • Millimeter to centimeter-sized CAIs grow locally in a short timescale (a few 100 to 10^4 years)
548 provided that the CAIs stick up to encounter velocities up to 10 m/s. High fragmentation
549 velocities, about 10m/s, do not seem unreasonable as experiments of cold dust coagulation
550 show that dust particles may stick up to velocities of around 1 m/s (Blum & Wurm, 2008).
551 Noting that at high temperatures CAIs become plastic, this would make collisions more
552 dissipative and thus more sticky (see e.g. Jacquet, 2014).
- 553 • The higher the temperature, the lower the dust/gas ratio and thus, the longer the timescale
554 to reach collisional equilibrium and the longer the growth timescale. The growth timescales
555 ranges from a few 100 years at ~ 1250 K to about 10^4 at ~ 1670 K. So, there is a complex cycle:
556 whereas CAIs may have been produced during 10^3 to 10^5 years, they are in an
557 accretion/destruction cycle with a timescale increasing with temperature. This constant
558 recycling may have important consequences on the chronology of CAIs as it scrambles
559 information between newly formed condensates and fragments of older CAIs, incorporated

560 into the same single object. This may bias estimates of bulk rock CAI ages toward older ages
561 and a more restricted period of formation.

562 • At lower temperatures, CAIs have a shorter growth timescale so that less refractory inclusions
563 are expected to be larger in average than more refractory inclusions. This is qualitatively
564 consistent with meteoritic observations.

565 Still a detailed comparison to laboratory data remains uneasy due to the few studies of the CAI size
566 distributions in the literature. In particular, it is unknown if various CAIs within a single chondrite
567 represent the full local size-distribution of CAIs in the environment in which they formed, or if some
568 aerodynamic processes could have yield to a preferential size sorting before or during incorporation
569 into a single chondrite (see e.g. Cuzzi et al., 2001; Johansen et al., 2007).

570 The numerical simulations presented in this work are, of course, limited by the omission of important
571 processes such as condensation from the gas and radial transport. Indeed, gas condensation produces
572 nanometer- to micrometer-sized precursors, which should feed the low-size end of the distribution.
573 The condensation at the surface of already formed CAIs may also slightly increase the body size. Due
574 to the local nature of the present simulation, loss of CAIs into the star is not considered here, and radial
575 transport may imply that a fraction of the biggest objects may disappear and be replenished due to
576 gas drag.

577 This study predicts that the growth of CAI through a simple coagulation/fragmentation competition,
578 starting from sub-micrometer condensates, naturally produces a simple power-law size distribution of
579 CAIs, that is indeed observed in CAIs cuts, as reported in the present paper. Advanced technics, like
580 3D tomography, may directly give access to the 3D size distribution of CAIs. We can note here that
581 Hezel et al. (2008) reported a Poisson distribution for CAIs in chondrites (using a 2D measurements).
582 Such a distribution, as noted by the authors, can be due to the fact that some areas of chondrites
583 studied contain only very few CAIs while others contain many of them. In our case, this effect of
584 heterogeneous distribution of CAIs within the whole rock is excluded because the sections observed

585 by Chaumard et al. (2014) and in the present paper (from 9.2 to 890 cm²) are several orders of
586 magnitude larger than those of Hezel et al. (2008) (<100 mm²).

587 If a simple-power law is not found using 3D tomography, this may mean that non-collisional processes
588 are at play during either (i) the formation of CAIs (ii) their accretion with the others chondritic
589 components (iii) or during their evolution inside the chondrite. For example, secondary alteration, like
590 metamorphism may result in selective destruction, or size modification, of the smallest or the most
591 fine-grained CAIs as discussed in section 4.3 and in Chaumard et al. (2014).

592 In conclusion, while CAIs may have experienced significant processing that may have erased many
593 signatures of their formation history, the sizes of these objects constrain their growth histories and the
594 conditions during which they grew in high-temperature regions of the solar nebula.

595

596 **Acknowledgements**

597 We thank M. Chaussidon for useful discussions. Two anonymous referees are thanked for valuable
598 comments that greatly improved the manuscript. We acknowledge the financial support of the
599 UnivEarthS Labex program at Sorbonne Paris Cité (ANR-10-LABX-0023 and ANR-11-IDEX-0005-02) and
600 of the French National Program of Planetology (PNP). E.T. acknowledges the support of “Région Ile de
601 France”. S.C. acknowledges support from the Institut Universitaire de France.

602 **References**

603 Aléon J., El Goresy A., and Zinner E., 2007. Oxygen isotope heterogeneities in the earliest protosolar
604 gas recorded in a meteoritic calcium-aluminum-rich inclusions. *Earth Planet Sci Lett* **263**, 114-127.

605 Aléon J., Marin-Carbonne J., McKeegan K. D. and El Goresy A. Multi-isotope study of the ultra-
606 refractory inclusion Efremovka 101.1 : inferences on ultra-high temperature processes in the solar
607 nebula. In preparation.

608 Amelin Y., Kaltenbach A., Izuka T., Stirling C. H., Ireland T. R., Petaev M., and Jacobsen S. B. 2010. U-
609 Pb chronology of the solar system's oldest solids with variable ²³⁸U/²³⁵U. *Earth and Planetary Science*
610 *Letters* **300**, 343–350.

- 611 Baillie K., Charnoz S., 2014. Time Evolution of a Viscous Protoplanetary Disk with a Free Geometry:
612 Toward a More Self-consistent Picture. *ApJ* **2014**, Id.35
- 613 Birnstiel, T., Dullemond, C.P., Brauer, F., 2010. Gas- and dust evolution in protoplanetary disks. *A&A*
614 **513**, id.A79
- 615 Birnstiel T., Ormel, C. W., Dullemond C. P., 2011. Dust size distributions in coagulation/fragmentation
616 equilibrium: numerical solutions and analytical fits. *A&A* **525**, id.A11
- 617 Blum J., Wurm G., 2008. The Growth Mechanisms of Macroscopic Bodies in Protoplanetary Disks *Ann.*
618 *Rev. Astron. Astroph.* **46**, 21-56
- 619 Bonal L., Quirico E., Bourot-Denise M. and Montagnac G., 2006. Determination of the petrologic type
620 of CV3 chondrites by Raman spectroscopy of included organic matter. *Geochim. Cosmochim. Acta* **70**,
621 1849-1863.
- 622 Bouvier A. and Wadhwa M. 2010. The age of the solar system redefined by the oldest Pb-Pb age of a
623 meteoritic inclusion. *Nature Geoscience* **3**, 637–641.
- 624 Brauer, F., Dullemond, C.P., Henning, T., 2008. Coagulation , fragmentation and radial motion of solid
625 particles in protoplanetary disks. *A&A* **480**, 859-877
- 626 Bullock E.M, MacPherson G.J., Nagashima K., Krot A.N., Petaev M.I., Jacobsen S.B. and Ulyanov A.A.,
627 2012. Forsterite-bearing Type B refractory inclusions from CV3 chondrites : from aggregates to
628 volatilized melt droplets. *Meteorit. Planet. Sci.* **47**, 2128-2147
- 629 Charnoz S., Fouchet L., Aléon J., Moreira M. 2011. Three-dimensional Lagrangian Turbulent Diffusion
630 of Dust Grains in a Protoplanetary Disk: Method and First Applications. *ApJ* **737**, Id.33
- 631 Charnoz S., Taillifet E., 2012. A Method for Coupling Dynamical and Collisional Evolution of Dust in
632 Circumstellar Disks: The Effect of a Dead Zone. *ApJ* **753**, Id.119
- 633 Chaumard N., Devouard B., Zanda B., Ferrière L., 2009. The link between CV and CK carbonaceous
634 chondrites based on parent body processes. *Meteorit. Planet. Sci.* **44**, A49
- 635 Chaumard N., Devouard B., Bouvier A., Wadhwa M., 2014. Metamorphosed calcium-aluminum-rich
636 inclusions in CK carbonaceous chondrites. *Meteorit. Planet. Sci.* **49**, 419–452.
- 637 Ciesla, F.J., 2010. The distributions and ages of refractory objects in the solar nebula. *Icarus* **208**, 455–
638 467
- 639 Connelly J. N., Bizarro M., Krot A. N., Nordlund A., Wielandt D. and Ivanova M. A., 2012. The absolute
640 chronology and thermal processing of solids in the solar protoplanetary disk. *Science* **338**, 651-655.
- 641 Cuzzi J.N., Hogan R.C., Paque J.M., Dobrolovski A.R., 2001. Size-selective Concentration of Chondrules
642 and Other Small Particles in Protoplanetary Nebula Turbulence. *ApJ* **546**, 496-508
- 643 Dohnanyi, J.W., 1969. Collisional model of asteroids and their debris. *J. Geophys. Res.* **74**, 2531-2554.
- 644 Ebel D.S., 2006. Condensation of rocky material in astrophysical environments. In *Meteorites and the*
645 *Early Solar System II*, eds D. S. Lauretta and H. Y. McSween, Univeristy of Arizon Press, Tucson, 253-
646 277.

Growth of CAIs

- 647 El Goresy A., Zinner E., Matsunami S., Palme H., Spettel B., Lin Y. and Nazarov M., 2002. Efremovka
648 101.1 : A CAI with ultrarefractory REE patterns and enormous enrichments of Sc, Zr, and Y in fassaite
649 and perovksite. *Geochim Cosmochim Acta* **66**, 1459-1491.
- 650 Estrada P.R., Cuzzi J. N., 2008. Solving the coagulation equation by the moment method. *ApJ* **682**, 515-
651 526
- 652 Fisher K. R., Tait A. W., Simon J. I. and Cuzzi J. N., 2014. Contrasting size distributions of chondrules
653 and inclusions in Allende CV3. Lunar and Planetary Science Conference, abstract #2711.
- 654 Fromang S., Papaloizou J., 2006. Dust settling in local simulations of turbulent protoplanetary disks.
655 *A&A* **452**, 751-762
- 656 Fromang S., Nelson R.P., 2009. Global MHD simulations of stratified and turbulent protoplanetary
657 discs. II. Dust settling. *A&A* **496**, 597-608
- 658 Fromang S., Lyra W., Masset F., 2011. Meridional circulation in turbulent protoplanetary disks. *A&A*
659 **534**, id. A107
- 660 Greenwood R. C., Franchi I. A., Kearsley A. T., and Alard O. 2010. The relationship between CK and CV
661 chondrites. *Geochimica et Cosmochimica Acta* **74**, 1684–1705.
- 662 Grossman L., 1972. Condensation in the primitive solar nebula. *Geochim. Cosmochim. Acta* **36**, 597-
663 619.
- 664 Hartmann W. K., 1969. Terrestrial, Lunar, and Interplanetary Rock Fragmentation. *Icarus* **10**, 201.
- 665 Hezel D.C., Russel S.S., Ross A.J., Kearsley A.T., 2008. Modal abundances of CAIs: Implications for bulk
666 chondrite element abundances and fractionations. *Meteorit Planet Sci* **43**, 1879-1894
- 667 Ivanova M. A., Krot A. N., Nagashima K. and MacPherson G. J., 2012. Compound ultrarefractory CAI-
668 bearing inclusions from CV3 carbonaceous chondrites. *Meteorit Planet Sci* **47**, 2107-2127.
- 669 Ivanova M. A., Lorenz C. A., Shuvalov V. V., Krot A. N., MacPherson G. J. and Bizarro M., 2014.
670 Plastically-deformed igneous Calcium-aluminum-rich inclusions from CV carbonaceous chondrites:
671 clues to a nature of CAI melting events. Lunar and Planetary Science Conference 45, abstract # 2166.
- 672 Jacquet, E., 2014. The quasi-universality of chondrule size as a constraint for chondrule formation
673 models. *Icarus* **232**, 176–186
- 674 Johansen, A., Oishi, J.S., Low, M. Mac, Klahr, H., Henning, T., 2007. Rapid planetesimal formation in
675 turbulent circumstellar discs. *Nature* **448**, 1022-1025
- 676 Kobayasho H., Tanaka H., 2010. Fragmentation model dependence of collision cascades. *Icarus* **206**,
677 735-746
- 678 Krot A. N., McKeegan K. D., Russell S S., Meibom A., Weisberg M., Zipfel J., Krot T. V., Fagan T. J. , Keil
679 K., 2001. Refractory calcium-aluminum-rich inclusions and aluminum-diopside-rich chondrules in the
680 metal-rich chondrites Hammadah al Hamra 237 and Queen Alexandra Range 94411. *Meteorit Planet
681 Sci* **36**, 1189-1216.
- 682 Kita N. T., Ushikubo T., Knight K. B., Mendybaev R. A., Davis A. M., Richter F. M. and Fournelle J. H.,
683 2012. Internal 26Al-26Mg isotope systematics of a type B CAI: Remelting of refractory precursor solids.
684 *Geochim. Cosmochim. Acta* **86**, 37-51.

Growth of CAIs

- 685 Kita N.T., Yin Q-Z, MacPherson G.J., Ushikubo T., Jacobsen B., Nagashima K., Kurahashi E., Krot A.N.,
686 Jacobsen S.B., 2013. ^{26}Al - ^{26}Mg isotope systematics of the first solids in the early Solar System. *Meteorit.*
687 *Planet. Sci.* **48**, 1383-1400
- 688 Krot A. N. , MacPherson G. J., Ulyanov A. A., and Petaev M. 2004. Fine-grained, spinel-rich inclusions
689 from the reduced CV chondrites Efremovka and Leoville : Mineralogy, petrology and bulk chemistry.
690 *Meteorit. Planet Sci.* **39**, 1517-1553
- 691 Krot A.N., Nagashima K., Wasserburg G.J., Huss G.R., Papanastassiou D., Davis A.M., Hutcheon I.D.,
692 Bizzarro M., 2014. Calcium-aluminum-rich inclusions with fractionation and unknown nuclear effects
693 (FUN CAIs): I. Mineralogy, petrology and oxygen isotopic composition. *Geochim. Cosmochim. Acta* **145**,
694 206-247
- 695 Kunihiro T., Nagashima K. and Yurimoto H., 2005. Microscopic oxygen isotopic
696 homogeneity/heterogeneity in the matrix of the Vigarano CV3 chondrite. *Geochim. Cosmochim. Acta*
697 **69**, 763-773.
- 698 Larsen K. K., Trinquier A., Paton C., Schiller M., Wielandt D., Ivanova M. A., Connelly J. N., Nordlund A.,
699 Krot A. N., and Bizarro M., 2011. Evidence for magnesium isotope heterogeneity in the solar
700 protoplanetary disk. *ApJ* **735**, L37
- 701 MacPherson G. J., 2003. Calcium-Aluminum-rich inclusions in chondritic meteorites. In. Meteorites,
702 Comets, and Planets, (ed. Davis A.M.), vol. 1 Treatise on geochemistry (eds H. D. Holland and K. K.
703 Turekian), Elsevier-Pergamon, Oxford, 201-246.
- 704 MacPherson G. J. and Grossman L. 1981. A once-molten, coarse-grained, Ca-rich inclusion in Allende.
705 *Earth Planet Sci Lett* **52**, 16-24.
- 706 MacPherson G. J. and Grossman L., 1984. « Fluffy » type A Ca-, Al-rich inclusions in the Allende
707 meteorite. *Geochim. Cosmochim. Acta* **48**, 29-46.
- 708 MacPherson G. J., Crozaz G. and Lundberg L.L., 1989. The evolution of a complex type B Allende
709 inclusion: An ion microprobe trace element study. *Geochim. Cosmochim. Acta* **53**, 2413-2427.
- 710 MacPherson G. J., Kita N. T., Ushikubo T., Bullock E. S. and Davis A. M. , 2012. Well-resolved variations
711 in the formation ages for Ca-Al-rich inclusions in the early solar system. *Earth Planet Sci Lett* **331-332**,
712 43-54.
- 713 Makide K. Nagashima K., Krot A. N. and Huss G. R. 2009. Oxygen isotopic compositions of solar
714 corundum grains. *ApJ* **706**, 142-147
- 715 Mathis J.S., Rumpl W., Nordsiek K.H., 1977. The size distribution of interstellar grains. *ApJ* **217**, 425-
716 433
- 717 Nakamura T. M., Sugiura N., Kimura M., Miyazaki A. and Krot A. N. 2007. Condensation and
718 aggregation of solar corundum and corundum-hibonite grains. *Meteorit. Planet. Sci.* **42**, 1249-1265.
- 719 Ormel C.W., Cuzzi J. N., 2007. Closed-form expressions for particle relative velocities induced by
720 turbulence. *A&A* **470**, 413-420
- 721 Park C., Nagashima K., Wasserburg G. J., Papanastassiou D. A., Hutcheon I.D., Davis A. M., Huss G. R.,
722 Bizzarro M. and Krot A. N., 2014. Calcium and Titanium isotopic compositions of FUN CAIs: Implications
723 for their origin. Lunar and Planetary Science Conference 45, abstract #2656.

Growth of CAIs

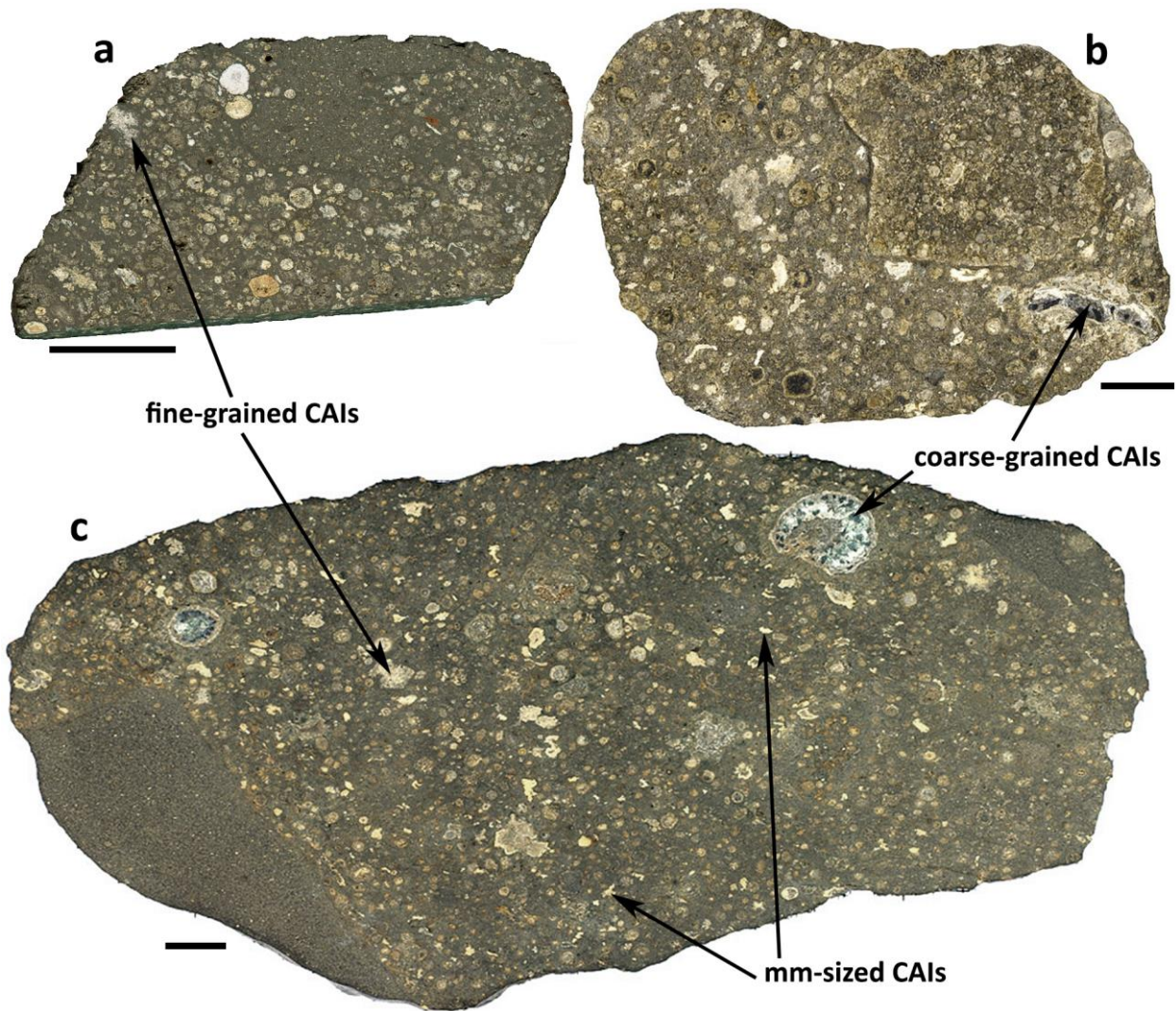
- 724 Rubin A. E., 2012. A new model for the origin of type-B and fluffy type-A CAIs : Analogies to remelted
725 compound chondrules. *Meteorit. Planet. Sci.* **47**, 1062-1074.
- 726 Simon S. B., Davis A. M. and Grossman L., 1999. Origin of compact type A refractory inclusions from
727 CV3 carbonaceous chondrites. *Geochim. Cosmochim Acta* **63**, 1233-1248.
- 728 Shakura N. I., and Sunyaev R. A., 1973. Black holes in binary systems. Observational appearance.
729 *Astronomy & Astrophysics* **24**, 337-355.
- 730
- 731 Shu F. H., Shang H., Glassgold A. E. and T. Lee, 1997. X-rays and fluctuating X-winds from protostars.
732 *Science* **277**, 1475-1479.
- 733 Tachibana S., Takigawa A., Miyake A., Nagahara H., Ozawa K., 2014. Condensation of forsterite under
734 controlled protoplanetary disk conditions. Lunar and Planetary Science Conference 45, abstract # 1226.
- 735 Takigawa A., Tachibana S., Nagahara H., and Ozawa K., 2012. Anisotropic evaporation and
736 condensation of circumstellar corundum. Lunar Planet Sci. Conf. 43, abstract #1875.
- 737 Tanaka H., Inaba S., Nakazawa K., 1996. Steady-State Size Distribution for the Self-Similar Collision
738 Cascade. *Icarus* **123**, 450-455
- 739 Taillifet E. Charnoz S., Aléon J., Baillié K, 2014. Formation of first solar systems solids in a turbulent
740 protoplanetary disk. To be submitted to ICARUS.
- 741 Takeuchi T., Lin D.N.C., 2002. Radial Flow of Dust Particles in Accretion Disks. *ApJ* **581**, 1344-1355
- 742 Thrane K., Bizarro M. and Baker J. A. 2006. Extremely brief formation interval for refractory inclusions
743 and uniform distribution of ²⁶Al in the early solar system. *ApJ* **646**, L159-L162.
- 744 Toppani A., Libourel G., Robert F. and Ghanbaja J., 2006. Laboratory condensation of refractory dust
745 in protosolar and circumstellar conditions. *Geochim Cosmochim. Acta* **70**, 5035-5060.
- 746 Wasson J. T., Isa J., and Rubin A. E. 2013. Compositional and petrographic similarities of CV and CK
747 chondrites: A single group with variations in textures and volatile concentrations attributable to impact
748 heating, crushing and oxidation. *Geochimica et Cosmochimica Acta* **108**, 45–62.
- 749 Youdin A.N., Lithwick Y., 2007. Particle stirring in turbulent gas disks: Including orbital oscillations.
750 *Icarus* **192**, 588-604.
- 751
- 752
- 753
- 754
- 755
- 756
- 757

FIGURES

758

759

760



761

762 **Figure 1:** Representative scanned slabs of CV and CK carbonaceous chondrites used to establish the
763 CAI size distributions in Chaumard et al. (2014) and the present study. (a) Allende, (b) NWA 2900, and
764 (c) TNZ 057. Scale bars are 1 cm. Numerous CAIs are visible as whitish inclusions, with several examples
765 of cm-sized and mm-sized CAIs labeled with arrows. Dark mm-sized grains of pyroxene are visible
766 within coarse-grained CAIs, whereas grains are indistinguishable in fine-grained CAIs.

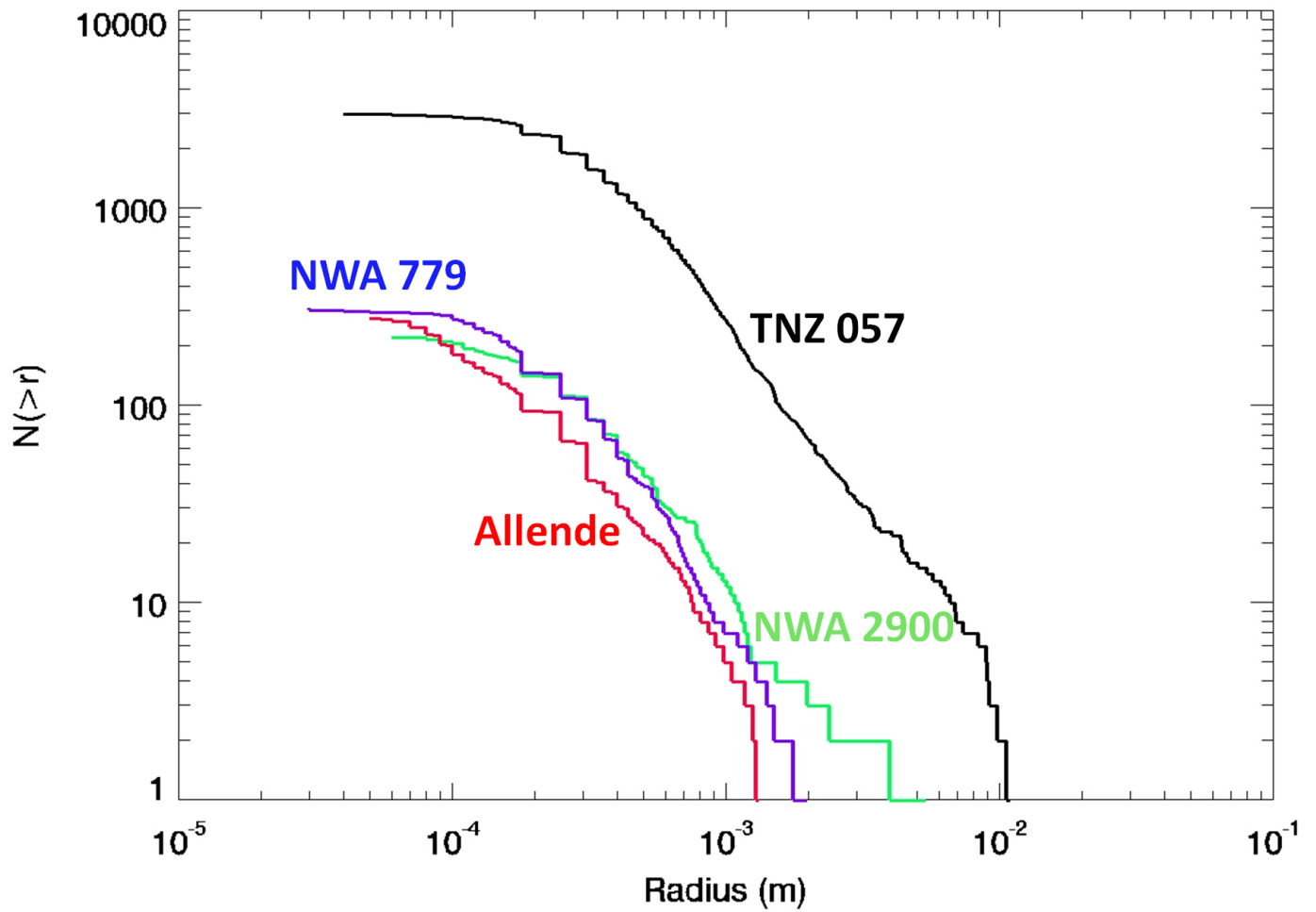
767

768

769

770

771



782

783 **Figure 2** : Cumulative size distribution (number of objects with radius larger than R) of CAIs measured

784 in different CV-CK carbonaceous chondrites: Allende (red), NWA 779 (blue), NWA 2900 (green), and

785 Tnz 057 (black).

786

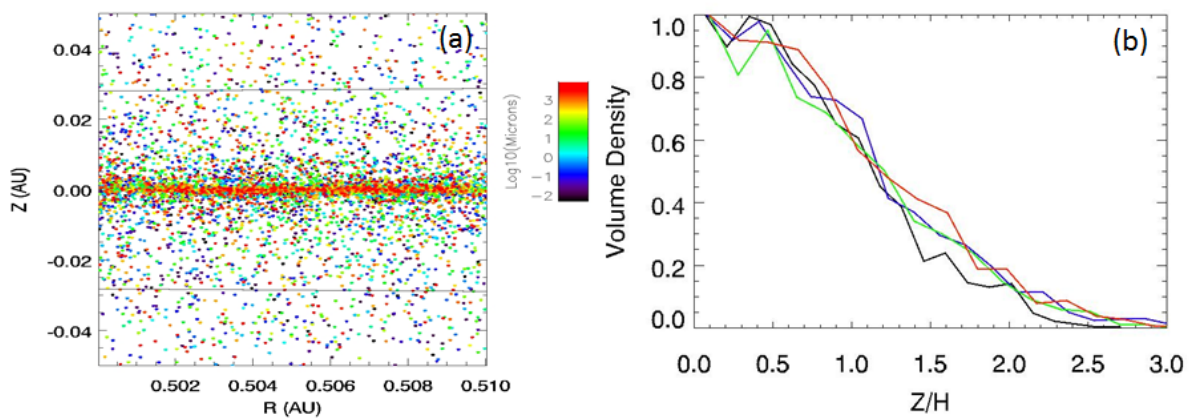
787

788

789

790

791
792
793
794
795
796
797

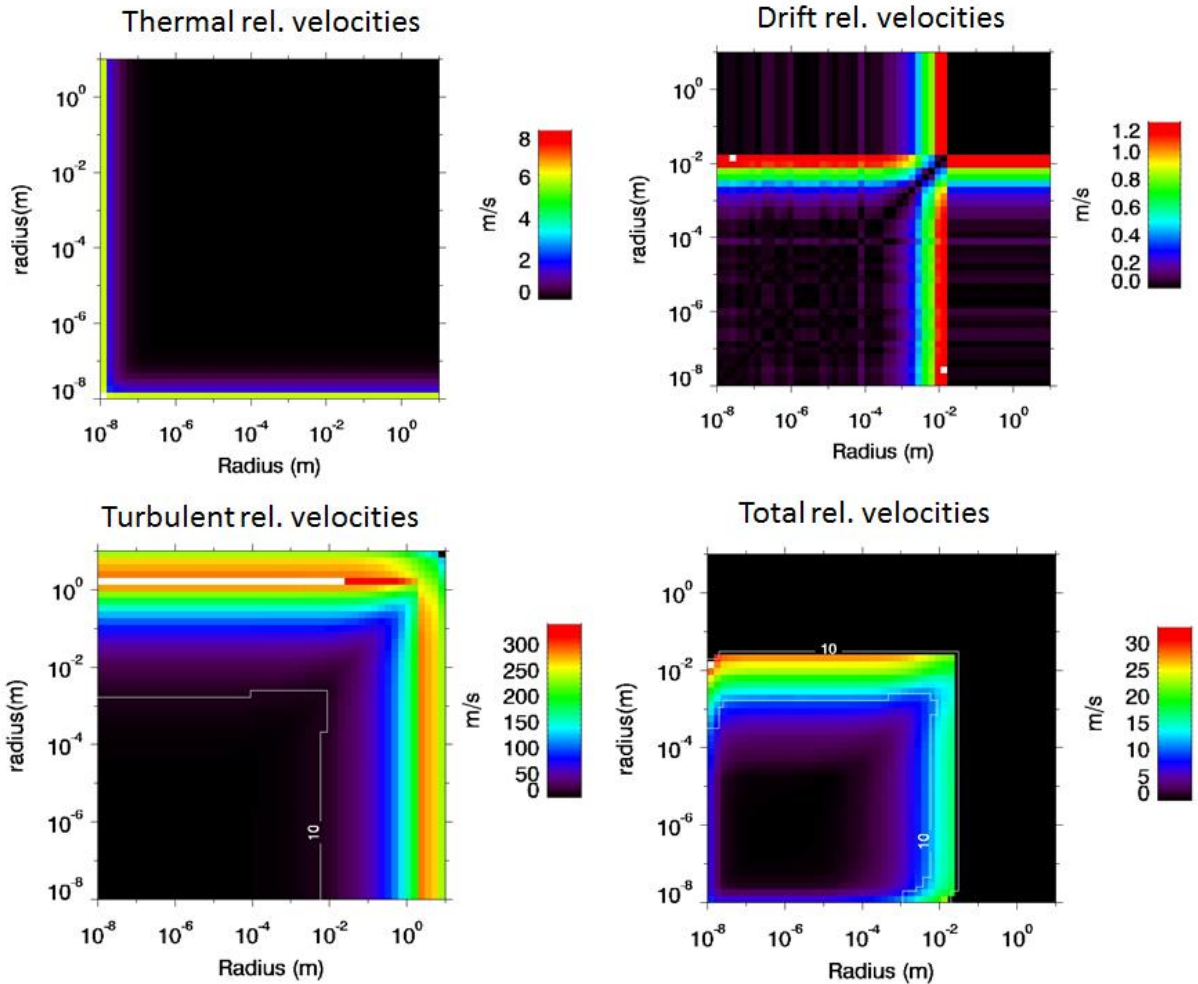


798
799

800 **Figure 3:** (a) (R,Z) positions of tracers in the disk, the color stands for the dust size (see scale on
801 right). Distance units are in astronomical units. The solid lines indicate the pressure scale height. (b)
802 Distribution of dust as a function of the distance above the midplane (Y axis) in units of pressure
803 scale height ($H \sim 0.026$ AU). Lines in black, blue, green, and red stand for CAIs with radii of 5000, 500,
804 50, and 5 microns, respectively. Each curve is normalized to 1 at its maximum. These plots are
805 extracted from simulation #5 (see table 2 for simulation parameters) after 1000 years of evolution.

806
807
808
809
810

811
812
813



814

815 **Figure 4:** Contribution of the different terms (thermal, turbulence, drift) to the total relative velocities
816 between pairs of particles, as a function of particle sizes. Here, the velocities are given for the particles
817 in the midplane of the disk. Note that the thermal and turbulent relative velocities are computed
818 analytically (section 3.2) whereas the drift velocities are directly measured in the simulation. The white
819 line designates encounter velocities of 10m/s.

820

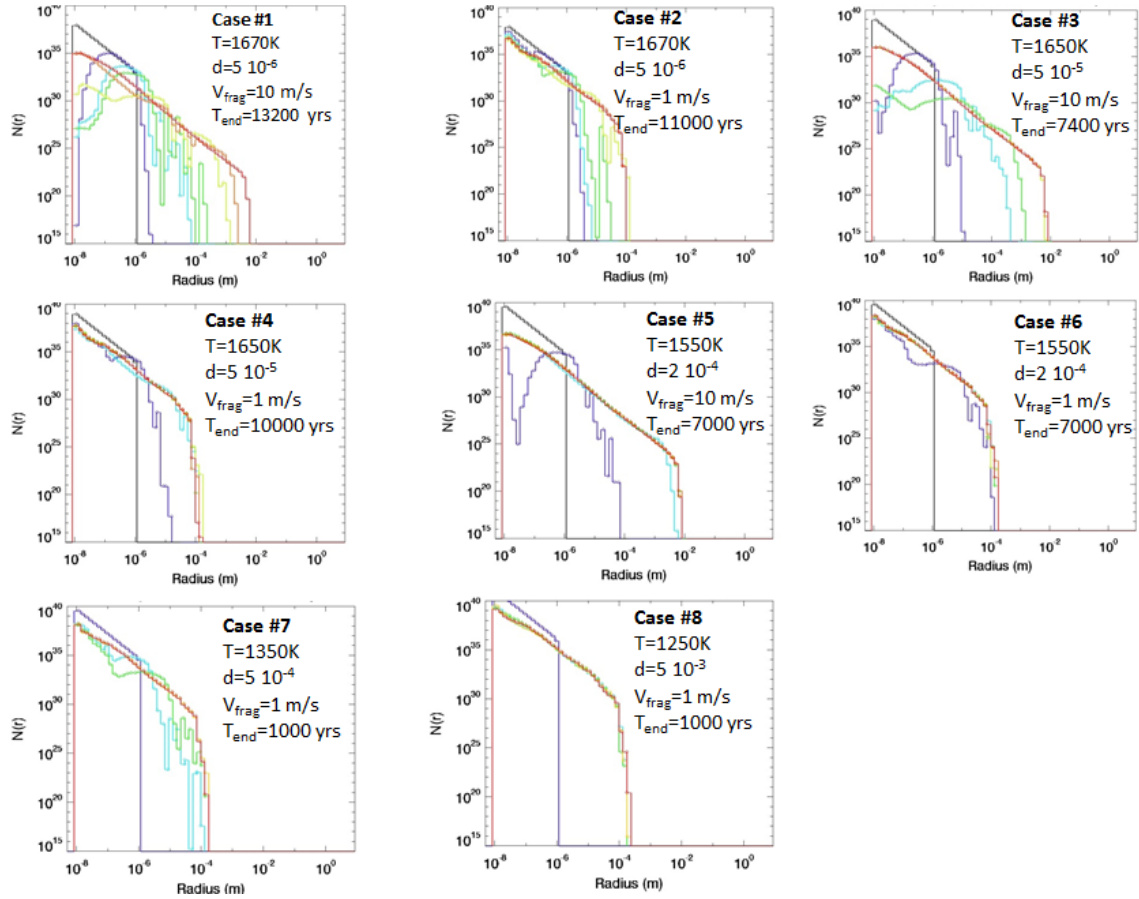
821

822

823

824

Growth of CAIs



825

826 **Figure 5:** Size distribution (number of bodies in each size bin) obtained in the different simulations
 827 cases (Table 2). Each simulation ends at a different time (T_{end}) after ensuring good convergence to a
 828 steady state. d stands for the dust/gas ratio. Color lines show the size distribution at different epochs:
 829 black: 0 years; dark-blue: $T_{\text{end}}/100$; light blue: $T_{\text{end}}/20$; green: $T_{\text{end}}/10$; yellow: $T_{\text{end}}/3$; orange: $T_{\text{end}}/2$;
 830 red: T_{end} .

Growth of CAIs

831

832

833

834

835

836

837

838

839

840

841

842

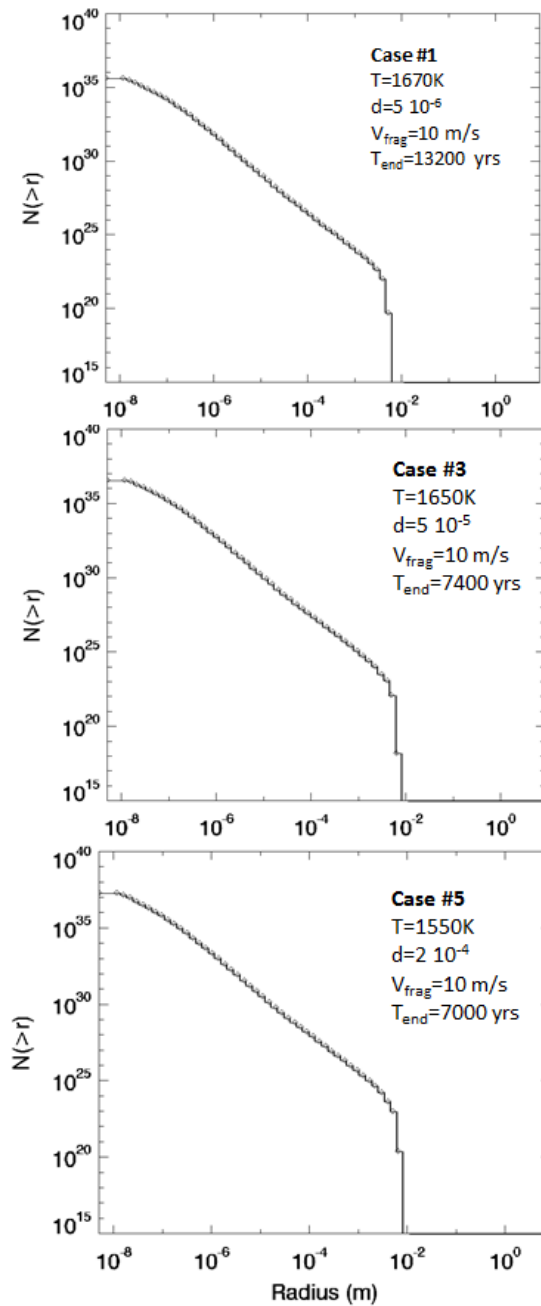
843

844

845

846

847

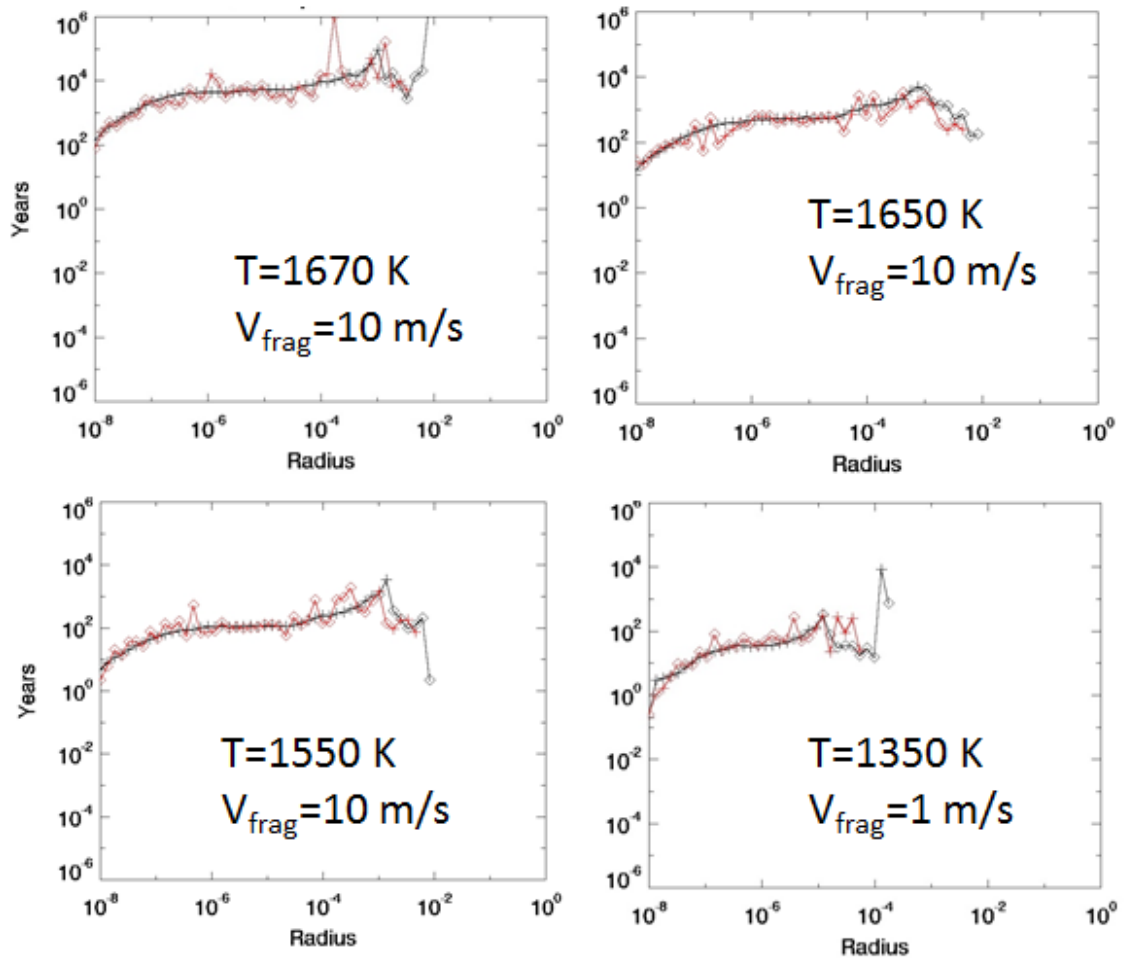


848 **Figure 6:** Cumulative size distributions obtained for $V_{frag}=10$ m/s at three different temperatures.

849 Cumulative distribution exponents varying between 0.1mm and 1 mm are reported in Table 2.

850

Growth of CAIs



851

852 **Figure 7:** Timescale for doubling/halving the mass in each size bin because of coagulation process (red
 853 line) or fragmentation process (black line). “+” symbol indicates a production rate (for coagulation this
 854 means that new bodies are formed due to coagulation, and for fragmentation this means that
 855 fragments are produced in the size range), diamonds indicate an elimination rate (for coagulation this
 856 means that bodies are used to form larger objects, and for fragmentation this means that bodies in
 857 the size range are destroyed). Spikes and discontinuities are due to the lack of numerical resolution
 858 and averaging only during one time-step.

859

860

861

Growth of CAIs

862

863

864

865

866

867

868

869

870

871

872

TABLES

873

Growth of CAIs

Meteorite Name	Petrologic type	Number of CAIs	R _{min} for fit	R _{max} for fit	Measured Exponent (cumulative size distrib)	1 sigma error	Corrected exponent assuming power law (-1)	Corrected exponent numerical correction (-0.84)
Tnz 057 (CK4)	> 4	3024	0.3 mm	7 mm	-1.70	± 0.004	-2.70	-2.54
NWA 2900 (CV3)	3.8–4	223	0.2 mm	2 mm	-1.71	± 0.021	-2.71	-2.55
NWA 779 (CV3)	3.6–3.8	311	0.2 mm	1.5 mm	-1.99	± 0.024	-2.99	-2.83
Allende (CV3ox)	> 3.6	278	0.2 mm	1 mm	-1.80	± 0.029	-2.8	-2.64

874

875 **Table 1** : Power-law exponents of CAI cumulative size distributions (so that $N(>r) \propto R^{\text{exponent}}$) measured
876 in different meteorites. R_{min} and R_{max} correspond to the lower and upper boundaries of CAI sizes over
877 which the slope has been measured. They were chosen so that the size distributions are about a power
878 law (i.e. appear as linear in Figure 2) in that range, so avoiding the knee at lower sizes (maybe due to
879 metamorphism) and the steep cut-off at larger sizes. “Sigma” shows the accuracy of the fit at 1 sigma.
880 The petrologic type quantifies the extent of parent body modifications due to metamorphism.
881 Primitive chondrites are of type 3.0. Increasing index corresponds to increasing metamorphism.
882 Complete chemical equilibration and partial melting are considered to occur at type 4 and above type
883 7, respectively. The given size exponents correspond to those directly measured on CAIs observed in
884 meteorites sections. Analytical corrected exponents are obtained by subtracting 1 to account for the
885 sectioning effect, assuming the size distribution is a power law (see Appendix A.1). Numerically

Growth of CAIs

886 corrected exponents are obtained by computing numerically the size-exponent between a real
887 distribution and the one observed in a meteorite cross-section, and may be somewhat more accurate
888 that the simple-power law correction (-1) for the size range close to the cut-off radius.

889

890

891

892

Run #	Gas Temperature	Dust/gas ratio (d)	Fragmentation Velocity
#1	1670 K	$5 \cdot 10^{-6}$	10 m/s
#2	1670K	$5 \cdot 10^{-6}$	1 m/s
#3	1650 K	$5 \cdot 10^{-5}$	10 m/s
#4	1650 K	$5 \cdot 10^{-5}$	1 m/s
#5	1550 K	$2 \cdot 10^{-4}$	10m/s
#6	1550 K	$2 \cdot 10^{-4}$	1 m/s
#7	1350 K	$5 \cdot 10^{-4}$	1 m/s
#8	1250 K	$5 \cdot 10^{-3}$	1 m/s

893

894 **Table 2:** List of the different simulation parameters investigated here. See section 3.1 for details.

895

896

897

898

899

900

901

902

903

904

905

906

907

Simulation Case	Exponent of the cumulative size distribution between 0.1mm and 1 mm	1 sigma error
#1 T=1670, $f=2 \cdot 10^{-6}$, $V_{\text{frag}}=10$ m/s	-2.43	± 0.026
#3 T=1650, $f=5 \cdot 10^{-5}$, $V_{\text{frag}}=10$ m/s	-2.44	± 0.032
#5 T=1550, $f=2 \cdot 10^{-4}$, $V_{\text{frag}}=10$ m/s	-2.44	± 0.04

908

909

910 **Table 3:** Measured slope exponents (cumulative size distribution) of the CAI cumulative size
 911 distribution obtained in simulations with $V_{\text{frag}}=10$ m/s. The slope exponent was measured from radii
 912 0.1mm to 1 mm in all cases.

913

914

915

916

917

918

919

920 **Appendix A: Relation between the apparent size distributions of CAIs** 921 **in sections across a meteorite and their real size distributions**

922 **A.1 Analytical correction assuming a simple power-law distribution**

923 CAIs' size distributions are obtained in laboratory from the observations of sections across a meteorite.
 924 In these sections only cut across CAIs are visible. So the apparent radii of these CAIs cuts are, of course,
 925 smaller than the real CAIs' radii. So an important question is: how the apparent size distribution of
 926 CAIs' radii observed in sections relates to the real distribution of CAIs' radii (if we could extract them
 927 from the meteorite)? We show here that if the real size distribution of CAIs is a power-law with
 928 exponent $-\alpha$ and if we consider a size range much smaller than the maximum size of CAIs, then the
 929 exponent of the CAIs' size distribution in the thin section is $-\alpha+1$ (so it is shallower). This is easily
 930 demonstrated below.

931 We assume that a collection of CAIs with a size distribution $P(R)$ is dispersed in a meteorite of
 932 characteristic length L and that all CAIs are spheres (as a first approximation) with radii R . We also
 933 assume that $P(R)$ follows a power-law:

$$934 \quad P(R) = KR^{-\alpha} \quad \text{Eq. A1}$$

935 with K standing for an arbitrary normalization factor and with $\alpha > 0$. dN , the number of CAIs with radius
 936 between R and $R+dR$, is:

$$937 \quad dN = P(R)dR \quad \text{Eq. A2}$$

938 We consider now a cut of the meteorite and we consider a single CAI with radius R . Let x be the distance
 939 of the cut plane to the CAI's center (measured perpendicularly to a cut plane). Cutting a sphere of
 940 radius R at the distance x from its center creates a disk with radius r given by:

$$941 \quad \begin{cases} r(x) = \sqrt{R^2 - x^2} \text{ for } x < R \\ r(x) = 0 \text{ for } x \geq R \end{cases} \quad \text{Eq. A3}$$

942

943 Let x_0 the abscissa of the CAI center in the meteorite. Noting that the meteorite's length is L , x may
 944 vary between x_0 and $L-x_0$. The probability of cutting the meteorite at distance x from the center, $P(x)$,
 945 is uniform so:

$$946 \quad P(x) = \frac{1}{L} \quad \text{Eq. A4}$$

947 Knowing that the distribution of x is uniform and considering a single CAI of radius R , what is the
 948 probability distribution of cutting the CAI and creating a disk with radius r ? We call this probability $P(r$
 949 $| R)$. By the classical law transformation of distribution, we must have $|| P(r) dr || = || P(x) dx ||$ so
 950 that:

$$951 \quad P(r | R) = P(x) \left| \left| \frac{dx}{dr} \right| \right| \quad \text{Eq. A5}$$

952 Knowing x as a function of r and R using Eq.A.3, we obtain:

$$953 \quad \begin{cases} P(r | R) = \frac{r}{L\sqrt{R^2-r^2}} f \text{ or } r < R \\ P(r | R) = 0 \text{ for } r \geq R \end{cases} \quad \text{Eq. A6}$$

954 Finally, we assume that we have a collection of CAIs in the meteorite with a radius probability
 955 distribution $P(R)$ given by Eq. A1. Now let assume we do a section of this meteorite, we want to know
 956 the distribution of CAI cuts with apparent radius r , $P(r)$. The probability of finding a CAI cut of apparent
 957 radius r is obtained by integrating $P(r | R)$ over all CAIs with radii R multiplied by the probability of
 958 finding a CAI with radius R , i.e:

$$959 \quad P(r) = \int_{R=0}^{+\infty} \frac{P(r|R)}{L\sqrt{R^2-r^2}} \cdot P(R) dR \quad \text{Eq. A7}$$

960 Noting that for $P(r | R)=0$ for $R < r$, we have:

$$961 \quad P(r) = \int_{R=r}^{+\infty} \frac{KrR^{-\alpha}}{L\sqrt{R^2-r^2}} dR \quad \text{Eq. A8}$$

962 Using a simple exchange of variable $U=R/r$ we find:

$$963 \quad P(r) = \frac{Kr^{-\alpha+1}}{L} \int_{U=1}^{+\infty} \frac{U^{-\alpha}}{\sqrt{U^2-1}} dU \quad \text{Eq. A9}$$

964 The term under the integral, whereas difficult to compute, does not depend on r . So we find:

$$965 \quad P(r) \propto r^{-\alpha+1} \quad \text{Eq.A10}$$

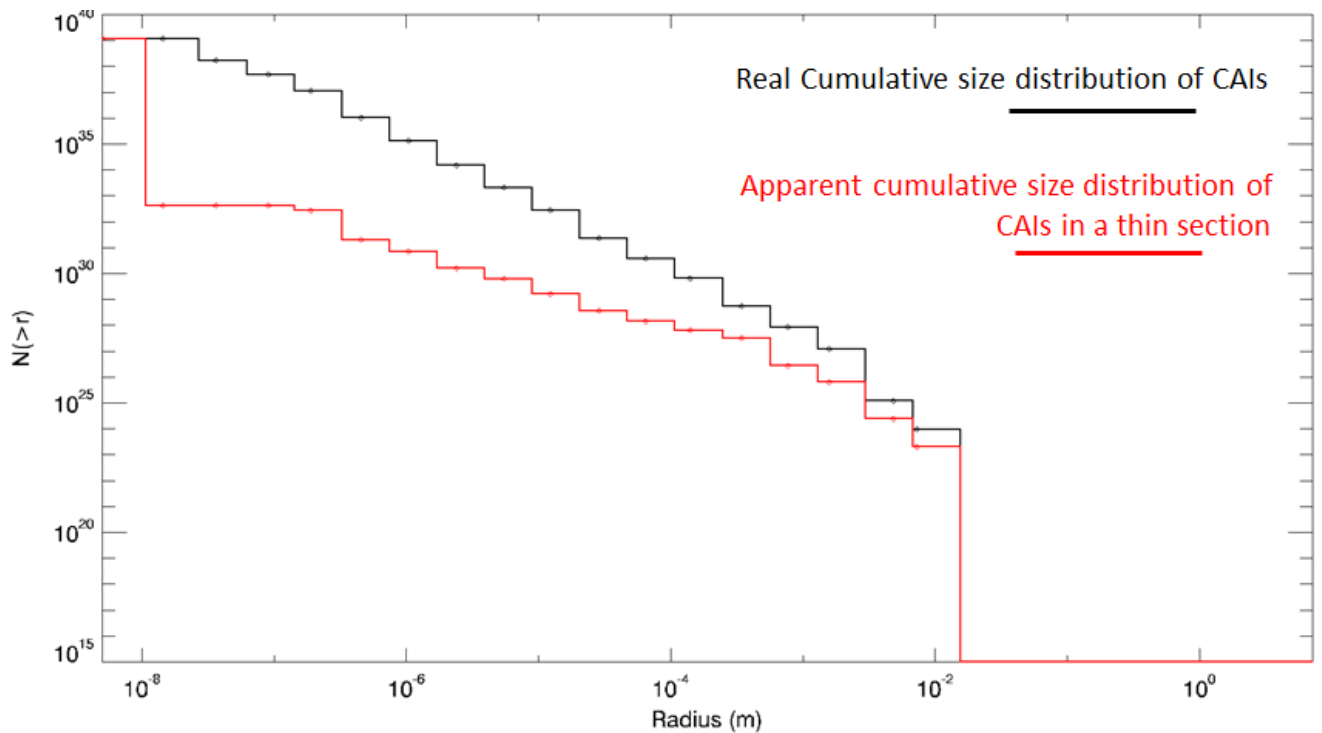
966 We see that the exponent of the distribution of CAIs' apparent radii in a meteorite section is *larger*
 967 than the real distribution of CAI radii. Since $\alpha > 0$, this means that the resulting distribution has a
 968 shallower slope. The difference between the two slopes is simply 1. To be fully convinced of this result
 969 we have simulated the process of "cutting" a meteorite numerically. We have spread in a volume of
 970 characteristic length L a distribution of CAIs. The distribution is shown Figure A1 in black solid line. We
 971 choose at random the abscissa of the cut plane in the meteorite and computed the apparent radius of
 972 CAIs in the resulting thin section using Eq.A3. Simulating 10^4 cuts like this, we averaged the resulting
 973 distributions (Figure A1, red line). Consistently with the calculus described above, it is found to be
 974 shallower with precisely a difference in slope by 1 in the size range between 10^{-7} and 10^{-3} m.

975 **A.2 Numerical correction below the cut-off radius.**

976 We have assumed above that the size-distribution of CAIs was a simple power-law. This is indeed a
 977 reasonable approximation of simulation's results. However, in the size range close to the cut-off radius
 978 (the size-range we are interested in, around 1 mm size), the size-distribution may deviate significantly
 979 from a power law because of the cut-off, inducing an error in the analytical correction described above.
 980 To overcome this difficulty, we have numerically simulated the process of "slicing" a meteorites using
 981 CAIs obtained in the numerical simulation: 10^4 "virtual" CAIs were distributed in a "virtual" meteorite
 982 (their centers were randomly choose using a uniform law) and a virtual cross-section was computed
 983 by choosing at random the cut-plane. Then, we computed the apparent radii of CAIs intersected by the
 984 cut-plane and computed the resulting size distribution. By doing so, we numerically determined that
 985 the correction factor between the real cumulative size distribution and the size-distribution in a cross-

986 section is about -0.84 ± 0.05 between 0.1 and 1mm for those size distributions that extend beyond
 987 1mm. This is close, but still substantially different from the analytical correction factor assuming a
 988 power law derived above (-1).

989



990

991 **Figure A1:** Computing numerically the distribution of CAI apparent radii in a thin section (red line) from
 992 an initial population of CAIs with distribution computed in black. To obtain the red distribution, we
 993 averaged over 10^4 different cuts drawn at random. The bump observed in the smallest size bins
 994 corresponds to all CAIs that did not appear in any section. The average slope of the black line is -2.42
 995 between $r=10^{-5}$ m and $r=10^{-3}$ m and the average slope of the red line is -1.37 in the same radial range.

996

997 **A.3 Summary**

998 **Describing the size-distribution as a single power-law is correct far from the size cut-off, whereas it**
 999 **fails close to the size cut-off (because the cut-off is more a step-like function, rather than a power**
 1000 **law).** In conclusion, if the real underlying size distribution of CAIs is a simple power law, extending up
 1001 to a maximum radius (here close to 1cm) the following correction to the observed size exponent should
 1002 be applied in order to retrieve the original size distribution of CAIs.

Growth of CAIs

- 1003
- In the range of sizes much below the maximum radius cut-off (so that the cut-off does not
- 1004
- 1005
- 1006
- For sizes close to the maximum cut-off radius, and especially just below, the correction is
- 1007
- 1008

1009 This change of regime is clearly visible in Figure A1 when comparing the red and black curve.

1010

1011

1012

1013